JPET Fast Forward. Published on June 17, 2020 as DOI: 10.1124/jpet.120.265868
This article has not been copyedited and formatted. The final version may differ from this version.

JPET # 265868

Slow tight binding inhibition of CYP17A1 by abiraterone redefines its kinetic selectivity and dosing regimen

Eleanor Jing Yi Cheong[1], Pramod C Nair[2], Rebecca Wan Yi Neo[1], Ho Thanh Tu[1], Fu Lin[3], Edmund Chiong[4,5], Kesavan Esuvaranathan[4,5], Hao Fan[6], Russell Z. Szmulewitz[7], Cody J. Peer[8], William D. Figg[8], Christina Li Lin Chai[1], John O Miners[2], Eric Chun Yong Chan[1,9]

[1]Department of Pharmacy, Faculty of Science, National University of Singapore, 18 Science Drive 4, Singapore 117543, Singapore; [2]Department of Clinical Pharmacology and Flinders Centre for Innovation in Cancer, College of Medicine and Public Health, Flinders University, Adelaide, Australia; [3]Bioinformatics Institute, Biotransformation Innovation Platform (BioTrans), Agency for Science, Technology and Research (A*STAR), 30 Biopolis Street, Singapore 138671; [4]Department of Surgery, National University Health System, 5 Lower Kent Ridge Road, Singapore 119074, Singapore; [5]Department of Urology, National University Hospital, 5 Lower Kent Ridge Road, Singapore 119074; [6]Bioinformatics Institute, Agency for Science, Technology and Research (A*STAR), 30 Biopolis Street, Singapore 138671; Department of Biological Sciences, National University of Singapore, 14 Science 23 Drive 4, Singapore 117543; Centre for Computational Biology, DUKE-NUS Medical School, 8 College Road, Singapore 169857; [7]The University of Chicago, Chicago, [8]National Cancer Institute, Rockville, MD, [9]National University Cancer Institute, Singapore (NCIS), NUH Medical Centre (NUHMC), 5 Lower Kent Ridge Road, Singapore 119074

Running title: Slow, tight binding inhibition of CYP17A1 by Abiraterone

Address correspondence to:

Professor Eric Chun Yong Chan, Department of Pharmacy, Faculty of Science, National University of Singapore, 18 Science Drive 4, Singapore 117543, Singapore.

Email: phaccye@nus.edu.sg; Telephone: +65-6516 6137; Fax: +65-6779155

Number of Text Pages	21
Number of Tables	1
Number of Figures	7
Number of References	59
Number of Words in the Abstract	249
Number of Words in the Introduction	841
Number of Words in the Discussion	1943

Abbreviations

AR	Androgen receptor
CYP17A1	Cytochrome P450 17A1
Δ^4 abiraterone	D4A
DHEA	Dehydroepiandrosterone
$t_{1/2}$	Half-life
k_1	Rate constant for the initial binding of inhibitor to enzyme
k_2	Rate constant for the dissociation of the initial EI complex
k_3	Forward isomerization rate constant for the conversion of EI to EI^*
k_4	Reverse isomerization rate constant for the conversion of EI^* to EI
$K_{i,app}$	Apparent inhibition constant for the initial EI complex
K_i	Inhibition constant for the initial EI complex
K_i^*	Inhibition constant for the final EI^* complex
k_{obs}	First order rate constant for onset of inhibition
mCRPC	Metastatic castration-resistant prostate cancer
mHSPC	Metastatic hormone-sensitive prostate cancer
MD	Molecular dynamics
PD	Pharmacodynamics
PK	Pharmacokinetics
PMF	Potential of mean force

Abstract

Substantial evidence underscores the clinical efficacy of inhibiting cytochrome P450 17A1 (CYP17A1)-mediated androgen biosynthesis by abiraterone for treatment of prostate oncology. Previous structural analysis and *in vitro* assays revealed inconsistencies surrounding the nature and potency of CYP17A1 inhibition by abiraterone. Here, we establish that abiraterone is a slow, tight binding inhibitor of CYP17A1, with initial weak binding preceding the subsequent slow isomerization to a high affinity CYP17A1-abiraterone complex (EI^*). The *in vitro* binding affinity of abiraterone to CYP17A1 (-12.8 kcal/mol for K_i^* = 0.39 nM) was quantitatively consistent with its *in silico* predicted binding free energy (-14.5 kcal/mol). Prolonged suppression of dehydroepiandrosterone (DHEA) concentrations observed in VCaP cells following abiraterone washout corroborated its protracted CYP17A1 engagement. Molecular dynamics simulations illuminated potential structural determinants underlying the rapid reversible binding characterizing the two-step induced fit model. Given the extended residence time (42 h) of abiraterone within the CYP17A1 active site, *in silico* simulations demonstrated sustained target engagement even when most abiraterone has been eliminated systemically. Subsequent pharmacokinetic-pharmacodynamic (PK-PD) modelling linking time-dependent CYP17A1 occupancy to *in vitro* steroidogenic dynamics predicted comparable suppression of downstream DHEA-sulphate at both 1000 and 500 mg doses of abiraterone acetate. This enabled mechanistic rationalization of a clinically reported PK-PD disconnect, where equipotent reduction of downstream plasma DHEA-sulphate levels was achieved despite a lower systemic exposure of abiraterone. Our novel findings provide the impetus for re-evaluating the current dosing paradigm of abiraterone, with the aim of preserving PD efficacy while mitigating its dose-dependent adverse effects and financial burden.

JPET Fast Forward. Published on June 17, 2020 as DOI: 10.1124/jpet.120.265868
This article has not been copyedited and formatted. The final version may differ from this version.

Significance Statement

With the advent of novel molecularly targeted anticancer modalities, it is becoming increasingly evident that optimal dose selection must necessarily be predicated on mechanistic characterization of the relationships between target exposure, drug-target interactions and pharmacodynamic endpoints. Nevertheless, efficacy has always been perceived as being exclusively synonymous with affinity-based measurements of drug-target binding. This work demonstrates how elucidating the slow, tight binding inhibition of CYP17A1 by abiraterone via *in vitro* and *in silico* analyses was pivotal in establishing the role of kinetic selectivity in mediating time-dependent CYP17A1 engagement and eventually downstream efficacy outcomes.

Introduction

Prostate cancer is ranked as the second most frequent cancer and the fifth leading cause of death among male malignancies worldwide (Bray *et al.*, 2018). Therapeutic interventions in prostate cancer are defined upon patient stratification into the clinical states continuum (Scher *et al.*, 2016). While localized prostate cancer remains amenable to curative interventions via radiation or surgery, androgen deprivation therapy (ADT) in the form of surgical or medical castration has become the standard of care in clinically advanced or disseminated disease. However, the initial response to ADT is often unsustainable and patients inevitably experience progression to castration-resistant prostate cancer (CRPC) within 2-3 years (Pienta and Bradley, 2006; Harris *et al.*, 2009). Metastases (mCRPC) are evident in ≥ 84% of diagnosed cases and prognosis is poor in mCRPC. Substantial evidence alludes to the reactivation of androgen receptor (AR)-mediated signalling as a key driver in disease progression despite castrate serum testosterone (< 50 ng/dL) levels (Mostaghel *et al.*, 2007). As a result, secondary hormonal manipulation via targeted molecular therapies has gained traction in the therapeutic management of mCRPC.

Bifunctional cytochrome P450 17A1 (CYP17A1), occupies a pivotal role in both adrenal and *de novo* intratumoral androgen biosynthesis, where it catalyzes sequential 17α-hydroxylation and C17,20 lyase reactions (**Figure 1A**) (Porubek, 2013). The resulting product dehydroepiandrosterone (DHEA) is a critical precursor for the downstream generation of potent AR ligands, testosterone and dihydrotestosterone. Consequently, abiraterone (administered as prodrug abiraterone acetate - AA) was first developed and approved in 2011 as a first in class CYP17A1 inhibitor to treat mCRPC (Vasaitis *et al.*, 2011; Yin and Hu, 2013). More recently, in men with metastatic hormone-sensitive prostate cancer (mHSPC), AA in combination with ADT was shown to significantly increase overall survival as compared to ADT monotherapy, culminating in the expansion of the clinical indications of AA to include the mHSPC patient population (Fizazi *et al.*, 2017).

AA is currently indicated to be administered at a dose of 1000 mg daily either 1 h before or 2 h after food (Janssen, 2019). Given that no dose limiting toxicities (DLTs) were detected up to 2000 mg in a Phase I dose escalation trial, the current dose selection was justified based on a plateau in anticipated

toxicities (i.e. upstream mineralocorticoid excess) observed at doses above 750 mg (Attard *et al.*, 2008). Implicit in this classical maximal tolerated dose (MTD) paradigm are the principles that 1) a linear dose-efficacy relationship exists and 2) toxicities are direct manifestations of exacerbated pharmacology. (Ji *et al.*, 2018). However, in a recent Phase II trial, comparisons of low-dose AA (LOW; 250 mg with a low-fat meal) versus standard dose AA (STD; 1000 mg fasting) demonstrated that despite trough abiraterone concentrations being significantly higher in the STD group compared to the LOW group, the extent of dehydroepiandrosterone-sulfate (DHEA-S) suppression was similar, verifying that the efficacy of CYP17A1 inhibition was preserved (Szmulewitz *et al.*, 2018). This observed pharmacokinetic-pharmacodynamic (PK-PD) uncoupling underscores how targeted therapeutics such as AA may achieve optimal antitumor activity at doses significantly lower than that required to elicit adverse outcomes. With the diminished utility of MTD-based strategies, rational dose selection for AA must instead be predicated on mechanistic and quantitative characterization of the relationships between target exposure, drug-target interactions and PD endpoints (Minasian *et al.*, 2014; Sachs *et al.*, 2016).

However, the mechanism of CYP17A1 inhibition by abiraterone has not been fully characterized. Firstly, X-ray crystal structures and spectral ligand binding assays reported coordination of the C17 pyridine of abiraterone with CYP17A1 heme iron, indicating a potent but reversible Type II interaction (DeVore and Scott, 2012). Garrido *et al* postulated that abiraterone is a slowly reversible CYP17A1 inhibitor and demonstrated its tight-binding effect with jump-dilution experiments (Garrido *et al.*, 2014). Furthermore, abiraterone was suggested to be a slow-binding inhibitor with enhanced inhibition upon pre-incubation with CYP17A1 (Jarman *et al.*, 1998). Collectively, the apparent complexities in the inhibition kinetics of CYP17A1 by abiraterone allude to a potential slow, tight binding phenomenon (**Figure 1B**). Consequently, both inhibitory potency (thermodynamic selectivity) and target occupancy (kinetic selectivity) by abiraterone against CYP17A1 must be explicitly considered when defining its *in vivo* drug activity.

Moreover, it was revealed that Δ^4-abiraterone (D4A) (**Figure 1C**), a downstream metabolite of abiraterone, inhibits multiple steroidogenic enzymes including CYP17A1 (Li *et al.*, 2015). The multi-targeting effects of D4A, coupled with its direct AR antagonism, has underscored its potential clinical utility in prostate oncology. Considering the structural similarities between abiraterone and D4A,

particularly the preservation of the pyridine ring, the inhibition kinetics of CYP17A1 by D4A are expected to be equally complex.

In this study, detailed *in vitro* biochemical and *in silico* molecular dynamics (MD) analyses allowed us to gain unprecedented insights into the kinetic and structural determinants of the abiraterone/D4A-CYP17A1 interaction. Utilizing a mechanistic PK-PD model, we subsequently demonstrated how the coupling between PK and the extended residence time of abiraterone within the CYP17A1 active site potentially plays a pivotal role in controlling time-dependent CYP17A1 occupancy and eventually downstream PD outcomes. Our findings could eventually guide the optimization of AA dosing across the continuum of prostate oncology.

Methods

Chemicals and Reagents. Abiraterone and DHEA were purchased from Tokyo Chemical Industry (Tokyo, Japan) while D4A was synthesized in-house (**Supplemental Methods and Supplemental Figure S1**). Prednisolone, progesterone, 17α-hydroxyprogesterone, 17α-hydroxypregnenolone, androstenedione, testosterone-2,3,4-$^{13}C_3$, ketoconazole and hydroxylamine hydrochloride were purchased from Sigma-Aldrich (St. Louis, MO). NADPH-regenerating system consisting of NADPH A (NADP+ and glucose 6-phosphate) and NADPH B (glucose-6 phosphate dehydrogenase) was purchased from BD Gentest (Woburn, MA). Dulbecco's modified eagle's medium (DMEM) high glucose, foetal bovine serum (FBS), 10× trypsin-EDTA and Hank's balanced salt solution (HBSS) were from Gibco® Life Technologies (Waltham, MA). 1 M stock solution of phosphate buffer saline (PBS) was from Vivantis (Subang Jaya, Malaysia). All other analytical reagents were of analytical grade.

Enzymes. Human CYP17A1R bactosomes containing recombinant human CYP17A1 (rCYP17A1) and human CYP-reductase enzymes supplemented with purified human cytochrome b5 were purchased from Cypex (Dundee, UK).

Slow Binding Inhibition Kinetics. To characterize the slow binding inhibition of CYP17A1 by abiraterone and D4A, pre-incubation time-dependence of reaction velocity was measured (Morrison and Walsh, 1988). Given the dual catalytic pathways associated with CYP17A1, both inhibition of progesterone 17α-hydroxylation and 17α-hydroxypregnenolone C17,20-lyase reactions were evaluated. Incubations (n=3) were performed in 96-well plates. Abiraterone or D4A (5-100 nM) was pre-incubated for 0-30 min at 37°C with rCYP17A1 (5 pmol/mL) and NADPH B in 50 mM potassium phosphate buffer (pH 7.4) containing 2 mM $MgCl_2$. Reactions were initiated by the addition of NADPH A and either 50 μM progesterone or 5 μM 17α-hydroxypregnenolone (saturating substrate conditions, **Supplemental Figure S2**) and allowed to proceed over the previously optimized incubation time of 20 min (**Supplemental Methods, Supplemental Figure S2**). 80 μL aliquots were subsequently removed and quenched with an equal volume of ice-cold acetonitrile containing the internal standard (prednisolone and androstenedione were utilized in the 17α-hydroxylase and C17,20-lyase inhibition assays respectively). The quenched samples were centrifuged at 2755 *g*, 4°C for 30 min and the supernatant

JPET Fast Forward. Published on June 17, 2020 as DOI: 10.1124/jpet.120.265868
This article has not been copyedited and formatted. The final version may differ from this version.

fraction was subjected to liquid chromatography tandem mass spectrometry (LC/MS/MS) analysis to determine the formation of 17α-hydroxyprogesterone or DHEA oxime, which were monitored as measures of residual enzyme activity. Oxime derivatization of DHEA and androstenedione prior to LC/MS/MS analysis is further described in the **Supplemental Material** and **Supplemental Figure S3**.

Semi-logarithmic plots illustrating the percentage of rCYP17A1 activity remaining (v/v_0) (relative to a [I] = 0 preincubation control sample) against pre-incubation time (t) were generated for the determination of the observed first-order rate constant for the onset of inhibition (k_{obs}) at various inhibitor concentrations (**Equation 1**) (Copeland, 2000, 2013).

$$ln(\frac{v}{v_0}) = -k_{obs} \cdot \mathrm{t} \quad \textbf{[1]}$$

Estimation of K_i, app for the Initial Encounter Complex. To obtain the apparent dissociation constant (K_i, app) for the initial CYP17A1-inhibitor encounter complex, procedures were similar to that of the pre-incubation time-dependent inhibition assays albeit without pre-incubation. The measured initial velocity (v_i) across various concentrations of abiraterone and D4A (1-300 nM) was normalized against the velocity of the uninhibited reaction (v_0). Data were fitted using standard four-parameter logistic models in GraphPad Prism 7.04 (San Diego, CA) as delineated in **Equation 2** to generate K_i, app (Copeland, 2013).

$$\frac{v_i}{v_0} = \frac{1}{1 + \frac{[I]}{K_i, app}} \quad \textbf{[2]}$$

Determination of K_i^* for the EI^* Complex. Using non-linear regression in GraphPad Prism 7.04 (San Diego, CA), the measured k_{obs} against $[I]$ was analyzed via a two-step inhibition mechanism as shown in **Figure 1B**, where the initial rapid binding of inhibitor to enzyme $[EI]$ is accompanied by subsequent slower isomerization to the final enzyme-inhibitor $[EI^*]$ complex (Copeland, 2013). **Equation 3a** was used to obtain the forward (k_3) and reverse kinetic constants (k_4) describing the slow binding inhibition. Given that k_4 reflects the rate limiting step for enzyme reactivation in the case of slow binding, the dissociation half-life for slow binding inhibitors could be calculated using **Equation 3b** (Copeland, 2013)**.**

JPET Fast Forward. Published on June 17, 2020 as DOI: 10.1124/jpet.120.265868
This article has not been copyedited and formatted. The final version may differ from this version.

$$k_{obs} = k_4 + \frac{k_3[I]}{K_i, app + [I]} \quad \textbf{[3a]}$$

$$Dissociation\ t_{1/2} = \frac{ln2}{k_{obs}} \approx \frac{ln2}{k_4} \quad \textbf{[3b]}$$

To determine the true values of K_i from experimental K_i, app, reversible inhibition assays were performed and Lineweaver-Burk transformations were used to discern the mode of inhibition (**Supplemental Methods**). Lastly the overall dissociation constants (K_i^*) of the EI^* complex, representing the true target affinity of inhibitor to CYP17A1, were determined using **Equation 4** (Copeland, 2013)**.**

$$K_i^* = \frac{K_i k_4}{k_3 + k_4} \quad \textbf{[4]}$$

Verifying the Functionality of the C17,20 Lyase Pathway in VCaP Cells. VCaP prostate cancer cells (ATCC® CRL-2876™) were purchased from American Type Culture Collection (ATCC) (Manassas, VA) and authenticated by ATCC. VCaP cells were cultured in DMEM media supplemented with 10% v/v FBS. For kinetic analyses, cells (passage numbers 8-16) were seeded in 24 well plates at a density of 0.4 million cells per well in a volume of 500 µL. Upon confluency, culture media was first removed, and each well was washed with PBS to minimize residual metabolic waste. Cells were incubated with media containing 17α-hydroxypregnenolone (2.5 to 45 µM, 1% v/v methanol). After 30 min, 200 µL aliquots of medium were collected, spiked with internal standard, and subjected to a two-step liquid-liquid extraction using methyl-tert butyl ether before concentration under nitrogen gas (**Supplemental Methods**). The dried residues were derivatized via reconstitution with 50 µL of 100 mM hydroxylamine hydrochloride solution (50% v/v methanol:water) and heated at 60°C for 1 h prior to LC/MS/MS measurement of DHEA oxime formation (Ming *et al.*, 2014). Subsequent assessment of inhibitor functionality involved the simultaneous co-incubation of inhibitors (abiraterone – 20 µM, 0.5% v/v methanol, ketoconazole – 25 µM, 0.5% v/v DMSO) or vehicle control along (0.5% v/v methanol/DMSO) with probe substrate (17α-hydroxypregnenolone - 30 µM, 0.6% v/v methanol) for 2 h before analysis of DHEA oxime formation.

Functional Recovery Experiments in VCaP Cells. Preincubation experiments utilizing VCaP cells were initiated by the addition of media containing abiraterone (40 μM, 1% v/v methanol), known reversible CYP17A1 inhibitor ketoconazole (40 μM, 1% v/v DMSO) along with vehicle controls (1% v/v methanol/DMSO). After 2 h, inhibitors were removed, and fresh media was added for the duration of the washout period (0 min, 30 min or 60 min). Finally, media containing the probe substrate, 17α-hydroxypregnenolone (30 μM, 1% v/v methanol) was added for 30 min. 200 μL aliquots of medium were collected and processed in the same manner as described in the previous section to measure DHEA oxime formation. At each time point (0 min, 30 min or 60 min), unpaired one tailed t-tests were applied to evaluate if the percentage recovery of maximal CYP17A1 activity (quantified by DHEA formation in the respective vehicle controls) following abiraterone pre-incubation and washout was significantly suppressed in comparison to ketoconazole treatment (p value < 0.05)

LC/MS/MS Measurement of Metabolite Formation. Samples were analyzed using an Agilent 1290 Infinity ultra-high-pressure liquid chromatography (Agilent Technologies, Santa Clara, CA) interfaced with AB Sciex QTRAP 5500 tandem mass spectrometry system (AB SCIEX, Framingham, MA). Injection volumes were 2 and 4 μL when quantifying 17α-hydroxyprogesterone and DHEA oxime production respectively. An ACQUITY UPLC ethylene bridged hybrid (BEH) C_{18}, 1.7 μM, 2.1 x 50 mm column (Waters, Milford, UA) was used for chromatographic separation. The aqueous mobile phases comprised 0.1% v/v formic acid in water (A) and 0.1% v/v formic acid in ACN (B). Mobile phases were delivered at 0.6 mL/min. The column and sample temperatures were maintained at 45°C and 4°C respectively. The gradient program was as follows: linear gradient from 20% to 60% B (0-0.5 min), isocratic at 60% B (0.5-1.5 min), linear gradient from 60% to 98% B (1.50-1.51 min), isocratic at 98% B (1.51-2 min), linear gradient from 98% to 20% B (2-2.01 min) and isocratic at 20% B (2.01-2.5 min). All analyses were performed in ESI positive mode. The MS source conditions were as follows: ion spray voltage +5500 V; source temperature 500°C; curtain gas 25 psi; GS1 (sheath gas) 30 psi; GS2 (drying gas) 30 psi; collision gas (nitrogen) medium. The compound-specific parameters are outlined in the **Supplemental Table S1** where the peak areas of 17α-hydroxyprogesterone and DHEA oxime were quantified as the products formed via 17α-hydroxylation and the C17,20-lyase reaction respectively. For cellular washout experiments, testosterone-2,3,4-$^{13}C_3$ was used as the internal standard. Chromatographic peak integration was performed using MultiQuant software (AB Sciex, Framingham,

MA) to obtain the peak area of the analyte expressed as a ratio to the peak area of IS (Peak Area Ratio - PAR).

MD Simulations. The X-ray crystal structure of abiraterone-bound CYP17A1 (PDB 3RUK, chain D) was used as the template for MD simulations and PMF calculations. All MD simulations of the protein and the heme prosthetic group were performed using GROMACS version 5.1.5 in conjunction with the GROMOS 54A7 force field (Schmid *et al.*, 2011; Abraham *et al.*, 2015). The simple point charge (SPC) water model was used to describe the solvent water. Simulations were performed under periodic boundary conditions in a rectangular box. A cut-off of 1.4 nm was applied to short-range non-bonded interactions, whereas long-range electrostatic interactions were calculated using the particle mesh Ewald (PME) algorithm (Darden *et al.*, 1993; Essmann *et al.*, 1995). Abiraterone was predicted to be neutral at pH 7.4 [ChemAxon, (Szegezdi and Csizmadia, 2007)]. Topology parameters for the neutral abiraterone were obtained using the Automated Topology Builder (ATB) and Repository (Malde *et al.*, 2011).

Abiraterone-bound CYP17A1 was placed in a cubic box of SPC water, including neutralizing counter ions. A steepest descents minimization followed by a position restraint simulation for 100 ps was performed under a constant volume (NVT) ensemble. A constant pressure (NPT) equilibration was performed for 100 ps using weak coupling to maintain pressure isotropically at 1.0 bar at a temperature of 310°K. A Parrinello-Rahman barostat was used to isotropically regulate pressure along with a Nosé–Hoover thermostat to maintain temperature, ensuring that a true NPT ensemble is sampled (Parrinello and Rahman, 1981; Nosé, 1984; Hoover WG, 1985). Production MD simulations were conducted for 250 ns without any restraints.

PMF Calculations. In order to calculate the binding free energy of abiraterone, PMF calculations of the abiraterone binding pathway from the CYP17A1 active site were performed along the central axis of the heme using the umbrella sampling method (Torrie and Valleau, 1977; Gordon *et al.*, 2013). The CYP17A1 structure was placed in a rectangular box with dimensions adequate to fulfil the minimum image convention and provide space for 'pulling' simulations to occur along the z-axis. The chosen reaction coordinate was defined as the axis passing through the heme, normal to the plane of the heme.

A harmonic restraint with a force constant of 1000 kJ/(mol·nm^2) was applied to the center of mass (COM) of abiraterone and moved along the reaction coordinate away from the core structure along the z-axis over 500 ps with a pull rate of 10 nm ns^{-1}. The pulling simulation was used to generate a set of 44 reference configurations (windows) separated by 0.05 nm intervals along the reaction coordinate. These windows were then used as starting configurations for umbrella sampling calculations. In each umbrella sampling simulation, the COM of abiraterone was harmonically restrained using a force constant of 1000 kJ/ (mol·nm^2) in the z-direction to allow sampling of a specific window along the reaction coordinate, where the motion of the abiraterone was not restrained in the xy-plane. MD simulations were performed for 20 ns with each window, providing a total simulation time of 880 ns for umbrella sampling.

The PMF profile was constructed using the weighted histogram analysis method (WHAM) (Kumar *et al.*, 1992; Hub *et al.*, 2010). The first 4 ns of each window are taken as equilibration and were therefore not included in the calculation of PMF values. The K_d was calculated from the PMF, W(z), using **Equation 5** (Chen and Chung, 2012)**,** where πr^2 is the cross-sectional area of the binding path, N_A is Avogadro's number, z_{min} and z_{max} are the z-positions of the abiraterone COM when fully bound to CYP17A1 and when in the bulk solvent, respectively. The radius R of the binding path was estimated as 0.5 nm based on the size of the heme porphyrin moiety.

$$K_d^{-1} = 1000\pi r^2 N_A \int_{Zmin}^{Zmax} \exp[-\mathrm{W(z)/kT}]\mathrm{dz} \quad \textbf{[5]}$$

ΔG for the binding of abiraterone to CYP17A1 was calculated using **Equation 6**, where ΔG is the binding free energy, R is the universal gas constant, T is the temperature, and K_d is the equilibrium dissociation constant.

$$\Delta G = -RT \ln K_d \quad \textbf{[6]}$$

The volume of the binding pocket was estimated using the mdpocket program (Schmidtke *et al.*, 2011). The pocket volume calculations were performed in an unliganded trajectory of CYP17A1-abiraterone simulation to estimate fluctuations in the presence of a bound ligand.

JPET Fast Forward. Published on June 17, 2020 as DOI: 10.1124/jpet.120.265868
This article has not been copyedited and formatted. The final version may differ from this version.

Development of a Mechanistic PK-PD Model Linking Abiraterone PK and CYP17A1-abiraterone Binding Kinetics to Steroidogenic Flux. We also sought to understand CYP17A1 target occupancy by abiraterone in the context of its *in vivo* PK (Dahl and Akerud, 2013). Considering the two-step slow binding inhibition mechanism as shown in **Figure 1B**, time-dependent changes in the concentration of each enzyme species (i.e. $[E]$, $[EI]$, $[EI^*]$) were simulated following a single 1000 mg or 500 mg dose of AA (Acharya *et al.*, 2012). Dynamic *in vivo* target occupancy was determined by the summation of $[EI]$ and $[EI^*]$.

Equations 7a-d describe the system of differential equations that were consecutively solved in parallel over very small intervals to simulate *in vivo* target occupancy (Vauquelin, 2017). The initial value of $[E]$ was defined as the steady state concentration of CYP17A1 *in vivo*. CYP17A1 has an abundance of approximately 35000 pmol/g tissue. Considering the weight (10 g) and volume of the adrenal glands (0.0085 L) gives a steady state concentration of 41 µM. The flux in the concentration of free inhibitor $[I]$ near the target was assumed to be equal to the plasma concentration time profile of abiraterone following AA administration.

$$\frac{d[E]}{dt} = k_{syn} - k_{deg}[E] + k_2[EI] - k_1[E][I] \quad \textbf{[7a]}$$

$$\frac{d[EI]}{dt} = k_1[E][I] - k_2[EI] + k_4[EI^*] - k_3[EI] \quad \textbf{[7b]}$$

$$\frac{d[EI^*]}{dt} = k_3[EI] - k_4[EI^*] \quad \textbf{[7c]}$$

$$Occupancy = [EI] + [EI^*] \quad \textbf{[7d]}$$

Supplemental Table S2 presents a summary of the relevant input parameters. Values for microscopic rate constants k_3 and k_4 were derived from the pre-incubation time-dependent kinetic experiments. As highlighted in **Equation 8a**, the overall target affinity (K_i^*) of abiraterone for CYP17A1 can be described as a composite of the various microscopic rate constants. With rearrangement, **Equation 8b** emphasizes the equivalence of $(k_3 + k_4)/ k_2$ and the $k_4/(k_1.K_i^*)$ ratios (Vauquelin, 2017).

JPET Fast Forward. Published on June 17, 2020 as DOI: 10.1124/jpet.120.265868
This article has not been copyedited and formatted. The final version may differ from this version.

$$K_i^* = \frac{k_2 k_4}{k_1(k_3 + k_4)} \quad \textbf{[8a]}$$

$$\frac{k_3 + k_4}{k_2} = \frac{k_4}{k_1 K_i^*} \quad \textbf{[8b]}$$

For induced fit binding, slow dissociation and high affinity rely on the stability of the $[EI^*]$, a scenario necessitating that k_4 becomes the kinetic bottleneck of the dissociation process (Copeland ***et al.***, 2006; Copeland, 2013; Vauquelin, 2017). Hence, to qualify as an induced fit binder, it follows that $(k_3 + k_4) \ll k_2$ and $k_4 \ll (k_1 K_i^*)$ (Vauquelin, 2017). Consequently, the eventual estimates of k_1 and k_2 satisfied these inequality relationships as well as the $K_{i,app}$ of the initial $[EI]$ complex obtained from kinetic analyses.

In subsequent PK-PD simulations, CYP17A1 engagement varying as a function of both abiraterone concentration and time was prospectively correlated with the extent of DHEA-sulphate suppression in a dynamic *in vitro* model of intracellular steroidogenesis as developed by Eldin ***et al.*** (Eldin et al., 2018) (**Supplemental Methods**). All analyses were performed in RStudio 1.1.456 using the deSolve package (R Core Team, 2013).

Correlating Abiraterone PK with Androgen Reduction. A Phase II trial by Szmulewitz *et al* demonstrated comparable efficacy of low dose abiraterone acetate (AA) (250 mg with a low-fat meal) to standard dose AA (1,000 mg fasting) (Szmulewitz ***et al.***, 2018). Utilizing plasma abiraterone measurements collected after 8 days of therapy (before and 2, 3, and 4 h after dosing) in the low dose and high dose groups, differences in PK parameters (i.e. area under the plasma concentration-time curve – $AUC_{0\text{-}4h}$ and peak plasma concentrations -- C_{max}) were evaluated and compared with AUC and C_{max} values derived from two Phase I trials (O'Donnell ***et al.***, 2004; Attard ***et al.***, 2008) studying the 500 mg dose of AA (fasted) in castrate patient cohorts. Group comparisons of log transformed PK data were performed via one-way analysis of variance, followed by Dunnett's multiple comparison test. Mean AUC and C_{max} ratios as well as 95% confidence intervals (CIs) for pairwise comparisons were calculated by retransformation of the logarithmic results.

JPET Fast Forward. Published on June 17, 2020 as DOI: 10.1124/jpet.120.265868
This article has not been copyedited and formatted. The final version may differ from this version.

Results

Abiraterone and D4A Cause Slow and Tight Binding Inhibition of CYP17A1. The binding of abiraterone and D4A to CYP17A1 was characterized by monitoring the formation of both 17α-hydroxyprogesterone and DHEA oxime as a function of pre-incubation time. Semi-logarithmic plots illustrated time- and concentration-dependent decreases in residual CYP17A1 activity (relative to a [I] = 0 preincubation control sample) and enabled determination of the first order rate constants for onset of inhibition (k_{obs}) at various concentrations of abiraterone (**Figures 2A** and **B**) and D4A (**Figures 2E** and **F**) using **Equation 1**. The hyperbolic dependence of k_{obs} on abiraterone/D4A concentration as observed in the kinetic plots (**Figures 2C**, **D**, **G** and **H**) is indicative of a two-step slow binding inhibition mechanism (**Figure 1B**) (Morrison and Walsh, 1988; Copeland, 2000). Concentration-dependent reduction of CYP17A1 activity in the absence of pre-incubation (y-intercept values in **Figures 2A**, **B**, **E** and **F**) further substantiates a two-step model, where the rapid, reversible binding of $E + I$ to form EI is manifested as an instantaneous effect on the initial reaction velocity (v_i). The apparent inhibition constant for the initial EI complex ($K_{i,}app$) was determined by fitting the dependence of fractional velocity (v_i/v_0) on inhibitor concentration using **Equation 2** (**Table 1**, **Figures 3A**, **B**, **E** and **F**). In the second step, the binding of abiraterone/D4A to CYP17A1 subsequently induces a time-dependent conformational change in CYP17A1 that results in a high affinity EI^* complex (**Figure 1B**). Non-linear regression analyses based on **Equation 3a** allowed the forward (k_3) and reverse (k_4) isomerization constants to be established (**Table 1**).

The Tight Inhibited Complex (EI^*) Demonstrates Significant Increases in Inhibitory Potency. Reversible inhibition of CYP17A1 by abiraterone (**Figures 3C** and **D**) and D4A (**Figures 3G** and **H**) was assessed. The intersection of lines above the x-axis in double reciprocal Lineweaver-Burk transformations revealed mixed mode inhibition of CYP17A1 by both abiraterone (**Supplemental Figures S4A** and **B**) and D4A (**Supplemental Figures S4C** and **D**). Hence, the $K_{i,}app$ values determined for abiraterone and D4A were corrected to the true K_i (**Table 1**). With acquisition of k_3, k_4 and K_i, the overall inhibition constants for the final EI^* complex ($K_i{}^*$) were calculated using **Equation 4**. For abiraterone and D4A, the isomerization of EI to EI^* was accompanied by significant increases in inhibitory potencies (K_i to $K_i{}^*$ in **Table 1**), expounding the thermodynamic stabilization of the ground state of EI^* versus EI (Tonge, 2018). Using **Equation 3b,** which assumes that k_4 is rate determining,

JPET Fast Forward. Published on June 17, 2020 as DOI: 10.1124/jpet.120.265868
This article has not been copyedited and formatted. The final version may differ from this version.

both abiraterone and D4A demonstrated prolonged residence time (>40 h) within the binding domain of CYP17A1 (**Table 1**). However, as reflected in **Table 1**, despite comparable inhibitory potencies across both 17α-hydroxylase and C17,20-lyase reactions, D4A exhibited longer residence time on CYP17A1 (95 h vs 29-42 h), highlighting the discordance between affinity and residence time measurements.

Binding free energy of the CYP17A1-abiraterone complex is consistent with kinetic analyses. Given the X-ray crystal structure reported by DeVore and Scott (DeVore and Scott, 2012) has abiraterone bound to CYP17A1, subsequent MD simulations considered the CYP17A1-abiraterone interaction only. The potential of mean force (PMF) profile was generated to predict the binding affinity of abiraterone to CYP17A1. In the reported binding mode (referred to hereafter pose A), the abiraterone steroid moiety orientates near perpendicular to the plane of the heme. Based on the PMF profile of abiraterone unbinding pathway, a distinct energy well occurs at the reaction coordinate, z = 5 Å (**Figure 4A**). The PMF calculations converged after 4ns; further extension of simulations to 20 ns for each umbrella window did not appreciably change the PMF profile nor binding free energy (SD = 0.5 kcal/mol). The binding mode associated with the energy well is essentially identical to that observed in the X-ray crystal structure, where the N atom of abiraterone forms a coordinate bond with heme Fe (< 2.6 Å). The computationally determined free energy of pose A was −14.5 kcal/mol and compares well to the experimental *in vitro* estimates (-12.5 and -12.8 kcal/mol for K_i^*= 0.42 nM and 0.39 nM depending on substrate, **Table 1**). Consistent with the PMF profile, only one abiraterone binding pose A is identified using this approach (**Figure 4B**).

Prolonged CYP17A1 binding of abiraterone was confirmed in cellular washout experiments. To ensure that any kinetic selectivity observed at the level of the purified recombinant CYP17A1 target could be qualitatively recapitulated in complex biological systems, cellular washout experiments utilizing human prostate cancer cells (VCaP) were performed. Formation of DHEA at various concentrations of 17α-hydroxypregnenolone exhibited Michaelis-Menten kinetics, establishing the cellular functionality of CYP17A1 (**Figure 5A**). In co-incubation experiments, both abiraterone (20 μM) and ketoconazole (25 μM) produced depressions of the maximal response observed after 2 h (quantified via DHEA formation in vehicle controls) (**Figure 5B**), demonstrating inhibition of C17,20-lyase reaction by abiraterone and ketoconazole. Upon pre-incubation of abiraterone and subsequent washout, continued suppression of

JPET Fast Forward. Published on June 17, 2020 as DOI: 10.1124/jpet.120.265868
This article has not been copyedited and formatted. The final version may differ from this version.

CYP17A1 activity was observed up to 60 min (**Figure 5C**). In contrast, minimal prolongation of DHEA suppression was observed following washout of known reversible CYP17A1 inhibitor ketoconazole (**Figure 5C**).

Identification of a second binding mode confirms the two-step induced fit binding mechanism observed in kinetic experiments. In addition to the tight binding mode, the kinetic experiments performed here identified a fast, reversible binding component of abiraterone to CYP17A1. Beyond the PMF calculations performed over a short simulation timescale, a long unrestrained MD simulation (250 ns) was performed to explore additional binding event(s). MD simulations of the abiraterone–CYP17A1 complex demonstrated two dominant binding modes of abiraterone within the active site. In pose A, the steroid moiety of abiraterone is oriented near vertically above the plane of the heme between the F and G helices. This is similar to the chemical interactions and orientation reported in the X-ray crystal structure (DeVore and Scott, 2012), and pose A observed in the PMF calculations (**Figure 4B**).

In the second binding mode, referred to as pose B, the plane of the steroid moiety is orientated parallel to the plane of the heme. The α-face of the steroid nucleus packs almost entirely along the I-helix, whereas in pose A, only a portion of the structure packs against the I-helix (**Figure 4C**). In pose A, H-bonding occurs between the 3β-OH group of abiraterone and Asn202. In pose B, H-bonding occurs between the 3β-OH group and Arg 239 (2.2 Å) and Asp 298 (2.4 Å) of the G and I helices, respectively. We propose that the binding mode of abiraterone identified in pose B may represent the fast, reversible interaction that occurs prior to heme coordination.

Simulated target occupancy after a single in vivo dose of abiraterone exceeds its pharmacokinetic (PK) half-life ($t_{1/2}$). Simulations of apparent CYP17A1 occupancy after a single 1000 mg or 500 mg dose of AA were performed using numerical integration over a system of differential equations for the two-step slow-binding enzyme inhibition mechanism (Vauquelin, 2017). The terminal elimination $t_{1/2}$ of abiraterone is approximately 16 h (**Figure 6A**). At the end of the dosing interval of 24 h, when most abiraterone has been eliminated systemically, an on-target peak to trough occupancy ratio (where trough is measured 24 h after dosing) was calculated to be 1.1 for both 1000 mg and 500 mg doses, indicating approximately constant apparent target occupancy between two consecutive

JPET Fast Forward. Published on June 17, 2020 as DOI: 10.1124/jpet.120.265868
This article has not been copyedited and formatted. The final version may differ from this version.

doses (Vauquelin, 2017). Notably, >80% apparent CYP17A1 engagement was preserved despite a dose reduction to 500 mg.

Translation of CYP17A1 Occupancy to PD Outcomes Rationalized a Clinically Observed PK-PD Disconnect. Nevertheless, the translation of target occupancy to efficacy outcomes requires additional consideration of the amount of target that must be complexed with abiraterone to elicit the desired PD effect (i.e. target vulnerability). When multiple dosing of AA for 72 h was utilized to perturb a baseline model of steroidogenesis, the model predicted comparable attenuations in intracellular DHEA-sulphate concentrations for the 1000 mg and 500 mg doses, calculated to be 3.26% and 4.68% at 72 h of baseline measurements (without inhibition) respectively (**Figure 6B**).

This PK-PD disconnect paralleled reported clinical findings from a Phase II trial comparing low-dose AA (250 mg q.d. with a low-fat meal) versus standard dose AA (1,000 mg q.d. fasting). The systemic exposure ($AUC_{0\text{-}4h}$) and C_{max} of abiraterone were significantly higher in the standard dose arm compared to the low dose group (**Figures 7A** and **B**), (mean $AUC_{0\text{-}4h}$ ratio = 2.08, 95% CI: 1.02 to 4.24; mean C_{max} ratio = 2.02, 95% CI: 1.01 to 4.05). Nevertheless, equipotent reduction of plasma DHEA-S levels was observed (Szmulewitz *et al.*, 2018), confirming that the clinical efficacy of CYP17A1 inhibition was maintained even at lower systemic exposure of abiraterone.

Notably, as presented in **Figure 7B**, comparable C_{max} measurements (mean C_{max} ratio = 0.98, 95% CI = 0.42 to 2.26) were observed between a 500 mg dose of AA administered under fasting conditions and 250 mg of AA administered with food. The mean AUC ($AUC_{0\text{-}12h}$ and $AUC_{0\text{-}72h}$) associated with the 500 mg dose was expectedly greater than $AUC_{0\text{-}4h}$ associated with the low dose treatment arm (mean AUC ratio = 2.83, 95% CI = 1.42 to 5.62) (**Figure 7A**). Based on PK measurements made up to 72 h in a Phase I dose escalation trial (Acharya *et al.*, 2012), the calculated $AUC_{0\text{-}4h}$ is approximately 50% of the total AUC across different doses. Taken together, a 500 mg dose of AA is expected to yield similar exposure to 250 mg of AA administered with food, representing a viable alternative to utilizing the food effect to enhance the systemic exposure of abiraterone.

Discussion

The translational disconnect between preclinical and clinical pharmacology is a perennial challenge. Incorrect assumptions underlying various processes in the causal chain between drug exposure and pharmacological response often restrict the success of *in vitro* to *in vivo* extrapolation (IVIVE) techniques. By elucidating the interaction between CYP17A1 and abiraterone/D4A, we demonstrate how inadequate characterization of target association-dissociation kinetics precludes an accurate determination of the *in vivo* time course of drug action.

For the first time, our results chronicle the profiling of abiraterone and its active metabolite D4A as slow, tight-binding inhibitors of steroidogenic CYP17A1 adhering to a two-step induced fit mechanism. As highlighted in **Table 1**, the conversion from the initial EI complex to the final EI* was accompanied by significant (> 50-fold) increases in inhibitory potencies (K_i to K_i^*) for both CYP17A1-mediated reactions. Hence, our results underscore how functional comparisons of compound inhibitory activity with the conventional assumption of rapid equilibrium may hinder detection of the time-dependent effects that is essential for holistic assessment of the true inhibitory potencies of non-classical inhibitors. Notably, the K_i and K_i^* values obtained largely reconcile the considerable incongruity observed in previous studies examining the nature and potency of CYP17A1 inhibition by abiraterone and D4A. K_i values quantifying the initial mixed mode inhibition of progesterone 17α-hydroxylation by abiraterone (50.7 nM) and D4A (23.4 nM) are comparable to those obtained by Garrido *et al* (K_i = 27 nM for abiraterone and 22 nM for D4A) (Garrido *et al.*, 2014). Conversely, spectral ligand binding assays monitoring time- and concentration-dependent heme coordination have implicated abiraterone and D4A as tight binding inhibitors with extremely high affinity for CYP17A1 (Garrido *et al.*, 2014). This alternative approach measures the dissociation of I from EI^* (K_d = 2.6 nM for abiraterone and < 1 nM for D4A) and is analogous to the K_i^* established in the present work (**Table 1**). Independently, PMF calculations from MD simulations yielded binding affinity estimates of abiraterone with CYP17A1 (-14.5 kcal/mol) that also verified the experimentally measured binding affinity (-12.5 and -12.8 kcal/mol for K_i^*= 0.42 nM and 0.39 nM). The convergence of results from MD simulations and biochemical analyses confirms the formation of the EI^* complex between abiraterone and CYP17A1.

Our kinetic experiments have confirmed that the high affinity interactions of abiraterone/D4A with CYP17A1 can be attributed to a two-step induced fit mechanism. However, the conservation of the global conformation of CYP17A1 in the presence of abiraterone (**Supplemental Figures S5A** and **B**), D4A (**Supplemental Figures S5C** and **D**) and various ligands (**Supplemental Figure S6**) (DeVore and Scott, 2012; Petrunak *et al.*, 2014, 2017) suggest that abiraterone or D4A can bind in the active site in the same orientation as that observed in the X-ray the crystal structure, which paradoxically renders the proposed induced fit mechanism untenable. Nevertheless, molecular docking simulations are by nature static and unable to simulate protein flexibility throughout binding (Salmaso and Moro, 2018). Indeed, CYP enzymes with large binding sites have been demonstrated to undergo dramatic conformational changes to accommodate and optimize the binding of ligands with diverse structures and shapes (Ekroos and Sjogren, 2006; Nair *et al.*, 2016; Sevrioukova and Poulos, 2017).

MD simulations demonstrated that the pyridine ring of abiraterone occupies an unfilled space of CYP17A1 between Val366 (on a K-L loop) and Val483 (β 4 loop) (DeVore and Scott, 2012) where its steroid nucleus binds near parallel to the plane of heme (pose B in **Figure 4C**). This parallel pose has been comparatively observed for steroidal ligands binding to CYP19A1 (e.g. PDB 3EQM, 5JKW;(Ghosh *et al.*, 2018)).

To probe the molecular basis of the two binding poses A and B, we investigated and established conformational changes in the F-helix (**Supplemental Table S3**) and the region connecting the F and G helices (Nair *et al.*, 2016) which are consistent with the secondary X-ray crystal structure of abiraterone-bound CYP17A1 (**Supplemental Figure S7**). Our MD simulations further demonstrated fluctuations of ligand-bound CYP17A1 active site volume (496 Å3 to 1023 Å3) with flexibilities noted for the F-helix, K-L loop and β4 loop region. Taken together, these conformational flexibilities possibly influence the binding modes of abiraterone.

In the X-ray crystal structure (pose A in **Figure 4A**), abiraterone binds to Asn202 (F-helix) within CYP17A1 active site via H-bonding while the roles of Arg239 and Asp298 were unclear (DeVore and Scott, 2012). It was observed during MD simulations that abiraterone adopts pose B when Arg239 (G-helix) and Asp298 (I-helix) are sufficiently close to form a salt-bridge (~3 Å), but abiraterone tends to

JPET Fast Forward. Published on June 17, 2020 as DOI: 10.1124/jpet.120.265868
This article has not been copyedited and formatted. The final version may differ from this version.

assume pose A as the distance between these residues increases. Tyr201 was found to be the most flexible side chain in the CYP17A1 binding site, with a RMSF value of 2.8 Å. The side chain dihedral angle of Tyr201, specifically χ1 (N-CA-CB-CG), repositions from a near gauche (~70°) to a near trans (~170°) conformation during simulations. This conformational rearrangement of Tyr201 favors the charge interaction between Arg239 and Asp298, and hence adoption of pose B. Thus, Tyr201, Arg239 and Asp298 play a crucial role in the reversible binding of abiraterone to CYP17A1. Collectively, MD simulations have provided insights into conformational adaptations within CYP17A1 that could justify the two predominant modes of abiraterone binding.

Apart from structural determinants, our findings underscore that equilibrium dissociation constants (thermodynamic selectivity) are not unequivocal indicators of the lifetime of drug-target complex (kinetic selectivity). This recognition has prompted the recent emergence of residence time ($1/k_{off} \approx 1/k_4$) as the paramount indicator of PD efficacy (Copeland *et al.*, 2006; Copeland, 2016; Tonge, 2018). Interpreting the prolonged residence time obtained for abiraterone in the context of previous dialysis and jump dilution studies demonstrates the validity of our estimates (Jarman *et al.*, 1998; Garrido *et al.*, 2014).

Nevertheless, the potential contribution of kinetic selectivity to *in vivo* efficacy remains complex due to dynamic changes in drug concentration, target turnover and the relationship between target occupancy and effect (i.e. target vulnerability) (Daryaee and Tonge, 2019). Selection of a 500 mg dose for comparison with the standard 1000 mg dose of AA was guided by results of a Phase 1 single dose study in castrate males, where target testosterone suppression was achieved and sustained for Days 2 to 5 post-therapy (O'Donnell *et al.*, 2004). Here, incorporating CYP17A1 turnover as well the plasma PK of abiraterone in relation to the lifetime of abiraterone-CYP17A1 complex, we first established that at both 1000 mg and 500 mg doses of AA, apparent protracted CYP17A1 engagement by abiraterone could be achieved *in vivo* (**Figure 6A**). In subsequent PK-PD simulations, dynamic CYP17A1 engagement was correlated with *in vitro* androgen suppression. Interestingly, we further demonstrated comparable attenuations in intracellular DHEA-S levels associated with both 1000 mg and 500 mg AA doses (**Figure 6C**). Taken together, our kinetic selectivity approach facilitated rationalization of a clinically observed PK-PD uncoupling highlighted by Szmulewitz *et al.* (Szmulewitz *et al.*, 2018) and

JPET Fast Forward. Published on June 17, 2020 as DOI: 10.1124/jpet.120.265868
This article has not been copyedited and formatted. The final version may differ from this version.

advocates a lower dosing requirement of abiraterone than that mandated by the MTD approach. Given that a 500 mg dose of AA administered fasted was shown to yield comparable PK with 250 mg of AA administered with a low-fat meal (**Figures 7A** and **B**), dose reduction could represent a viable alternative to circumvent the high variability in oral bioavailability that often accompanies the food effect in drug PK.

With abiraterone slated for treating newly-diagnosed high risk mHSPC, its average duration of treatment could span up to 24 months (Fizazi *et al.*, 2017). Therefore, the pharmacoeconomic implications of any potential dose reduction could be substantial as abiraterone acetate has an approximate retail cost of USD 10,000 per month (Szmulewitz *et al.*, 2018). Moreover, the inhibition of the 17α-hydroxylase reaction by abiraterone has been shown to produce dose-dependent mineralocorticoid-related toxicities that necessitates concomitant prednisone administration. Hence, potential dose reductions could also be instrumental in enhancing the safety of abiraterone therapy.

It is important to note that apparent occupancy-time profiles (**Figure 6A**) were generated on the assumption of equivalent total tissue and plasma concentrations. This approach deviates from that advocated by the free drug hypothesis, where drug molecules bind to plasma and tissue proteins, resulting in a reduction in free, pharmacologically active concentrations necessary for target engagement. Based on the free drug theory, with assumptions of steady state PK and the dominance of passive diffusion processes, the unbound partition coefficient ($K_{p,uu}$) for a non-eliminating tissue will equal unity ($C_{u,t}/C_{u,p}$= ~1) (Zhang *et al.*, 2019). Expectedly, when unbound plasma concentrations were utilized as a surrogate for unbound tissue concentrations to effect CYP17A1 engagement, the extent of CYP17A1 occupancy over time was significantly diminished (**Supplemental Figure S8A**). Nevertheless, in the case of abiraterone, we believe that asymmetry of free drug concentrations between target tissues and plasma at steady state is a distinct possibility. Firstly, corroborating Mostaghel *et al*, our preliminary analyses demonstrated potential organic anion transporting polypeptide (OATP)1B3-mediated abiraterone uptake (**Supplemental Figure 8B**) (Mostaghel *et al.*, 2017). Coupled with evidence supporting increased expression of OATP1B3 in metastatic lesions from prostate cancer, intratumoural levels of abiraterone could be reasonably higher than that predicted by $K_{p,uu}$ (Schulte and Ho, 2019). Additionally, another key assumption underpinning the free drug hypothesis is that

interactions between the drug and the receptor are reversible. Consequently, concentration gradient can be the sole factor invoked to describe free drug permeation. However, with the tight binding of abiraterone to CYP17A1, it is possible that with adequate abiraterone concentrations exceeding the target covalent binding threshold, a separate concentration gradient can be re-established with the excess free abiraterone (Zhang *et al.*, 2019). This postulation is also supported by distribution studies performed in rats, where the highest ^{14}C-abiraterone concentrations detected within the adrenal gland were 15-35 times the corresponding blood concentration (European Medicines Agency, 2011). Taken together, there remains considerable uncertainties in occupancy determinations due to the inability to accurate estimate the molar ratio of intracellular free abiraterone versus CYP17A1. As such, the threshold and strength of correlation between target occupancy and effect as described by a target vulnerability function remains poorly defined. Consequently, direct quantification of *in vivo* target engagement via imaging techniques such as positron emission tomography becomes imperative to inform and correct estimates of apparent CYP17A1 occupancy.

In the case of D4A, residence time effects were also expected given the prolonged CYP17A1 engagement observed in *in vitro* kinetic analyses. Nevertheless, prolongation of phenotypic response after D4A washout was not observed (data not shown). This apparent incongruity could be attributed to the susceptibility of the Δ4,3-keto structure of D4A to irreversible 5α-reduction and 5β-reduction within the tumour microenvironment (Li *et al.*, 2016). In fact, direct incubation of D4A in LAPC4 prostate cancer cell line for 48 h demonstrated substantial downstream conversion of D4A to the initial 5α-reduced metabolite (3-keto-5α-abiraterone), which is similarly present at higher concentrations than D4A in patients with mCRPC taking abiraterone (Li *et al.*, 2016). Hence, it is possible that the elimination of D4A is not rate-limiting, diminishing the utility of a prolonged residence time in extending its PD durability (Dahl and Akerud, 2013).

In conclusion, this study provides compelling evidence that abiraterone is a slow, tight-binding inhibitor of steroidogenic CYP17A1. Our *in vitro* enzyme kinetic analyses provided quantitative description of pertinent kinetic parameters characterizing the two-step binding that are entirely consistent with the results of MD simulations. Cellular washout experiments provided further corroborative evidence for the protracted residence time of abiraterone on CYP17A1. In addition, MD simulations offered insights into

the fast, reversible step preceding tight binding that was not apparent from both X-ray crystallography and molecular docking simulations. The long dissociation $t_{1/2}$ of both abiraterone and D4A reflects protracted residence time on CYP17A1, which in turn creates the awareness that the incorporation of residence time along with PK parameters is imperative in the mechanistic PK-PD modeling of abiraterone to optimize mCRPC pharmacotherapy.

Acknowledgements

This research was undertaken with the assistance of resources from the National Computational Infrastructure (NCI), which is supported by the Australian Government. The authors also acknowledge Flinders University's High Performance Computing resources for this work.

Authorship Contributions

Participated in research design:	Cheong, Nair, Neo, Tu, Lin, Fan, Miners and Chan
Conducted experiments:	Cheong, Nair, Neo, Tu, Lin, Fan, Miners and Chan
Contributed new reagents:	Tu and Chai
Performed data analysis:	Cheong, Nair, Neo, Tu, Lin, Fan, Szmulewitz, Peer, Figg, Miners and Chan
Wrote or contributed to the writing of the manuscript:	Cheong, Nair, Neo, Tu, Lin, Chiong, Esuvaranathan, Fan, Chai, Miners and Chan

References

Abraham MJ, Murtola T, Schulz R, Páll S, Smith JC, Hess B, and Lindahl E (2015) GROMACS: High performance molecular simulations through multi-level parallelism from laptops to supercomputers. *SoftwareX* **1**–**2**:19–25.

Acharya M, Bernard A, Gonzalez M, Jiao J, De Vries R, and Tran N (2012) Open-label, phase I, pharmacokinetic studies of abiraterone acetate in healthy men. *Cancer Chemother Pharmacol* **69**:1583–1590.

Attard G, Reid AHM, Yap TA, Raynaud F, Dowsett M, Settatree S, Barrett M, Parker C, Martins V, Folkerd E, Clark J, Cooper CS, Kaye SB, Dearnaley D, Lee G, and de Bono JS (2008) Phase I clinical trial of a selective inhibitor of CYP17, abiraterone acetate, confirms that castration-resistant prostate cancer commonly remains hormone driven. *J Clin Oncol* **26**:4563–4571.

Bray F, Ferlay J, Soerjomataram I, Siegel RL, Torre LA, and Jemal A (2018) Global cancer statistics 2018: GLOBOCAN estimates of incidence and mortality worldwide for 36 cancers in 185 countries. *CA Cancer J Clin* **68**:394–424.

Chen R, and Chung S-H (2012) Binding Modes and Functional Surface of Anti-mammalian Scorpion α-Toxins to Sodium Channels. *Biochemistry* **51**:7775–7782.

Copeland RA (2013) Slow Binding Inhibitors, in *Evaluation of Enzyme Inhibitors in Drug Discovery* pp 203–244, John Wiley & Sons, Inc., Hoboken, NJ, USA.

Copeland RA (2016) The drug-target residence time model: A 10-year retrospective. *Nat Rev Drug Discov* **15**:87–95.

Copeland RA (2000) Time-Dependent Inhibition, in *Enzymes: A Practical Introduction to Structure, Mechanism, and Data Analysis* pp 318–349.

Copeland RA, Pompliano DL, and Meek TD (2006) Drug–target residence time and its implications for lead optimization. *Nat Rev Drug Discov* **5**:730–739.

Dahl G, and Akerud T (2013) Pharmacokinetics and the drug-target residence time concept. *Drug Discov Today* **18**:697–707.

Darden T, York D, and Pedersen L (1993) *Particle Mesh Ewald: An Nlog (N) Method for Ewald Sums in Large Systems*.

Daryaee F, and Tonge PJ (2019) Pharmacokinetic–pharmacodynamic models that incorporate drug–target binding kinetics. *Curr Opin Chem Biol* **50**:120–127.

DeVore NM, and Scott EE (2012) Structures of cytochrome P450 17A1 with prostate cancer drugs abiraterone and TOK-001. *Nature* **482**:116–119.

Ekroos M, and Sjogren T (2006) Structural basis for ligand promiscuity in cytochrome P450 3A4. *Proc Natl Acad Sci* **103**:13682–13687.

Essmann U, Perera L, Berkowitz ML, Darden T, Lee H, and Pedersen LG (1995) A smooth particle mesh Ewald method. *J Chem Phys* **103**:8577–8593.

European Medicines Agency (2011) Assessment Report For Zytiga (abiraterone).

Fizazi K, Tran N, Fein L, Matsubara N, Rodriguez-Antolin A, Alekseev BY, Özgüroğlu M, Ye D, Feyerabend S, Protheroe A, De Porre P, Kheoh T, Park YC, Todd MB, Chi KN, and LATITUDE Investigators (2017) Abiraterone plus Prednisone in Metastatic, Castration-Sensitive Prostate Cancer. *N Engl J Med* **377**:352–360.

Garrido M, Peng HM, Yoshimoto FK, Upadhyay SK, Bratoeff E, and Auchus RJ (2014) A-ring modified steroidal azoles retaining similar potent and slowly reversible CYP17A1 inhibition as abiraterone. *J Steroid Biochem Mol Biol* **143**:1–10.

Ghosh D, Egbuta C, and Lo J (2018) Testosterone complex and non-steroidal ligands of human aromatase. *J Steroid Biochem Mol Biol* **181**:11–19.

Gordon D, Chen R, and Chung S-H (2013) Computational Methods of Studying the Binding of Toxins From Venomous Animals to Biological Ion Channels: Theory and Applications. *Physiol Rev* **93**:767–802.

Harris WP, Mostaghel EA, Nelson PS, and Montgomery B (2009) Androgen deprivation therapy: Progress in understanding mechanisms of resistance and optimizing androgen depletion. *Nat Clin Pract Urol* **6**:76–85.

Hoover WG (1985) Canonical dynamics: Equilibrium phase-space distributions. *Phys Rev A, Gen Phys* **31**:1695–1697.

Hub JS, de Groot BL, and van der Spoel D (2010) g_wham—A Free Weighted Histogram Analysis Implementation Including Robust Error and Autocorrelation Estimates. *J Chem Theory Comput* **6**:3713–3720.

Janssen (2019) ZYTIGA® (abiraterone acetate) Highlights of Prescribing Information.

Jarman M, Barrie SE, and Llera JM (1998) The 16,17-double bond is needed for irreversible inhibition of human cytochrome p45017alpha by abiraterone (17-(3-pyridyl)androsta-5,16-dien-3beta-ol, 1) and related steroidal inhibitors. *J Med Chem* **41**:5375–5381.

Ji Y, Jin JY, Hyman DM, Kim G, and Suri A (2018) Challenges and Opportunities in Dose Finding in Oncology and Immuno-oncology. *Clin Transl Sci* **11**:345–351.

Kumar S, Rosenberg JM, Bouzida D, Swendsen RH, and Kollman PA (1992) THE weighted histogram analysis method for free-energy calculations on biomolecules. I. The method. *J Comput Chem*

13:1011–1021.

Li Z, Alyamani M, Li J, Rogacki K, Abazeed M, Upadhyay SK, Balk SP, Taplin M-E, Auchus RJ, and Sharifi N (2016) Redirecting abiraterone metabolism to fine-tune prostate cancer anti-androgen therapy. *Nature* **533**:547–551.

Li Z, Bishop AC, Alyamani M, Garcia JA, Dreicer R, Bunch D, Liu J, Upadhyay SK, Auchus RJ, and Sharifi N (2015) Conversion of abiraterone to D4A drives anti-tumour activity in prostate cancer. *Nature* **523**:347–51.

Malde AK, Zuo L, Breeze M, Stroet M, Poger D, Nair PC, Oostenbrink C, and Mark AE (2011) An Automated Force Field Topology Builder (ATB) and Repository: Version 1.0. *J Chem Theory Comput* **7**:4026–4037.

Minasian L, Rosen O, Auclair D, Rahman A, Pazdur R, and Schilsky RL (2014) Optimizing dosing of oncology drugs. *Clin Pharmacol Ther* **96**:572–579.

Ming DS, Pham S, Deb S, Chin MY, Kharmate G, Adomat H, Beheshti EH, Locke J, and Guns ET (2014) Pomegranate extracts impact the androgen biosynthesis pathways in prostate cancer models in vitro and in vivo. *J Steroid Biochem Mol Biol* **143**:19–28.

Morrison JF, and Walsh CT (1988) The behavior and significance of slow-binding enzyme inhibitors., in *Advances in enzymology and related areas of molecular biology* (Meister A ed) pp 201–301, John Wiley & Sons, Inc., New York, USA.

Mostaghel EA, Cho E, Zhang A, Alyamani M, Kaipainen A, Green S, Marck BT, Sharifi N, Wright JL, Gulati R, True LD, Loda M, Matsumoto AM, Tamae D, Penning TN, Balk SP, Kantoff PW, Nelson PS, Taplin ME, and Montgomery RB (2017) Association of tissue abiraterone levels and SLCO genotype with intraprostatic steroids and pathologic response in men with high-risk localized prostate cancer. *Clin Cancer Res* **23**:4592–4601.

Mostaghel EA, Page ST, Lin DW, Fazli L, Coleman IM, True LD, Knudsen B, Hess DL, Nelson CC, Matsumoto AM, Bremner WJ, Gleave ME, and Nelson PS (2007) Intraprostatic androgens and androgen-regulated gene expression persist after testosterone suppression: Therapeutic implications for castration-resistant prostate cancer. *Cancer Res* **67**:5033–5041.

Nair PC, McKinnon RA, and Miners JO (2016) Cytochrome P450 structure–function: insights from molecular dynamics simulations. *Drug Metab Rev* **48**:434–452.

Nosé S (1984) A unified formulation of the constant temperature molecular dynamics methods. *J Chem Phys* **81**:511–519.

O'Donnell A, Judson I, Dowsett M, Raynaud F, Dearnaley D, Mason M, Harland S, Robbins A, Halbert G, Nutley B, and Jarman M (2004) Hormonal impact of the 17α-hydroxylase/C17,20-lyase inhibitor abiraterone acetate (CB7630) in patients with prostate cancer. *Br J Cancer* **90**:2317–2325.

Parrinello M, and Rahman A (1981) Polymorphic transitions in single crystals: A new molecular dynamics method. *J Appl Phys* **52**:7182–7190.

Petrunak EM, DeVore NM, Porubsky PR, and Scott EE (2014) Structures of human steroidogenic cytochrome P450 17A1 with substrates. *J Biol Chem* **289**:32952–32964.

Petrunak EM, Rogers SA, Aubé J, and Scott EE (2017) Structural and functional evaluation of clinically relevant inhibitors of steroidogenic cytochrome P450 17A1. *Drug Metab Dispos* **45**:635–645.

Pienta KJ, and Bradley D (2006) Mechanisms underlying the development of androgen-independent prostate cancer. *Clin Cancer Res* **12**:1665–1671.

Porubek D (2013) CYP17A1: a biochemistry, chemistry, and clinical review. *Curr Top Med Chem* **13**:1364–84.

R Core Team (2013) R: a language and environment for statistical computing., R Found. Stat. Comput., Vienna, Austria.

Sachs JR, Mayawala K, Gadamsetty S, Kang SP, and Alwis DP De (2016) Optimal Dosing for Targeted Therapies in Oncology : Drug Development Cases Leading by Example. **22**:1318–1325.

Salmaso V, and Moro S (2018) Bridging Molecular Docking to Molecular Dynamics in Exploring Ligand-Protein Recognition Process: An Overview. *Front Pharmacol* **9**:923.

Scher HI, Morris MJ, Stadler WM, Higano C, Basch E, Fizazi K, Antonarakis ES, Beer TM, Carducci MA, Chi KN, Corn PG, de Bono JS, Dreicer R, George DJ, Heath EI, Hussain M, Kelly WK, Liu G, Logothetis C, Nanus D, Stein MN, Rathkopf DE, Slovin SF, Ryan CJ, Sartor O, Small EJ, Smith MR, Sternberg CN, Taplin M-E, Wilding G, Nelson PS, Schwartz LH, Halabi S, Kantoff PW, Armstrong AJ, and Prostate Cancer Clinical Trials Working Group 3 (2016) Trial Design and Objectives for Castration-Resistant Prostate Cancer: Updated Recommendations From the Prostate Cancer Clinical Trials Working Group 3. *J Clin Oncol* **34**:1402–1418.

Schmid N, Eichenberger AP, Choutko A, Riniker S, Winger M, Mark AE, and van Gunsteren WF (2011) Definition and testing of the GROMOS force-field versions 54A7 and 54B7. *Eur Biophys J* **40**:843–856.

Schmidtke P, Bidon-Chanal A, Luque FJ, and Barril X (2011) MDpocket: open-source cavity detection and characterization on molecular dynamics trajectories. *Bioinformatics* **27**:3276–3285.

Schulte RR, and Ho RH (2019) Organic anion transporting polypeptides: Emerging roles in cancer pharmacology. *Mol Pharmacol* **95**:490–506.

Sevrioukova IF, and Poulos TL (2017) Structural basis for regiospecific midazolam oxidation by human cytochrome P450 3A4. *Proc Natl Acad Sci U S A* **114**:486–491.

Szegezdi J, and Csizmadia F (2007) Calculating the pKa Values of Small and Large Molecules., in

American Chemical Society Spring meeting p.

Szmulewitz RZ, Peer CJ, Ibraheem A, Martinez E, Kozloff MF, Carthon B, Harvey RD, Fishkin P, Yong WP, Chiong E, Nabhan C, Karrison T, Figg WD, Stadler WM, and Ratain MJ (2018) Prospective International Randomized Phase II Study of Low-Dose Abiraterone With Food Versus Standard Dose Abiraterone In Castration-Resistant Prostate Cancer. *J Clin Oncol* **36**:1389–1395.

Tonge PJ (2018) Drug-Target Kinetics in Drug Discovery. *ACS Chem Neurosci* **9**:29–39.

Torrie GM, and Valleau JP (1977) Nonphysical sampling distributions in Monte Carlo free-energy estimation: Umbrella sampling. *J Comput Phys* **23**:187–199.

Vasaitis TS, Bruno RD, and Njar VCO (2011) CYP17 inhibitors for prostate cancer therapy. *J Steroid Biochem Mol Biol* **125**:23–31.

Vauquelin G (2017) Distinct *in vivo* target occupancy by bivalent- and induced-fit-like binding drugs. *Br J Pharmacol* **174**:4233–4246.

Yin L, and Hu Q (2013) CYP17 inhibitors—abiraterone, C17,20-lyase inhibitors and multi-targeting agents. *Nat Rev Urol* **11**:32–42.

Zhang D, Hop CECA, Patilea-Vrana G, Gampa G, Seneviratne HK, Unadkat JD, Kenny JR, Nagapudi K, Di L, Zhou L, Zak M, Wright MR, Bumpus NN, Zang R, Liu X, Lai Y, and Khojasteh SC (2019) Drug Concentration Asymmetry in Tissues and Plasma for Small Molecule–Related Therapeutic Modalities. *Drug Metab Dispos* **47**:1122–1135.

Footnotes

This work was supported by the Singapore Ministry of Education Tier 1 Academic Research Funding [Grant R-148-000-249-114] and the National University of Singapore (NUS) President's Graduate Fellowship (PGF) to E.J.Y.C and the National University of Singapore, Department of Pharmacy, Final Year Project Funding provided to R.W.Y.N. F.L. and H.F. gratefully acknowledge the financial support from Biomedical Research Council (BMRC) of A*STAR, Singapore

Figure Legends

Figure 1. Clinical utility of abiraterone and D4A in prostate cancer (mCRPC). (**A**) Endogenous androgen biosynthesis pathway showing the inhibitory effects of abiraterone/D4A on CYP17A1. (**B**) Schematic describing the two proposed mechanisms of slow, tight binding inhibition of CYP17A1 by abiraterone/D4A (**C**) Chemical structures of abiraterone and D4A where the latter is formed via metabolism of abiraterone by 3β-hydroxysteroid dehydrogenase (3βHSD).

Figure 2. Pre-incubation time-dependent inhibition of CYP17A1 by abiraterone and D4A. Semi-logarithmic plots illustrate time- and concentration-dependent inhibition of CYP17A1 by (**A** and **B**) abiraterone or (**E** and **F**) D4A using progesterone and 17α-hydroxypregnenolone as probe substrates for 17α-hydroxyprogesterone and dehydroepiandrosterone formation respectively. The relationship between the observed first-order rate constants for the onset of inhibition (k_{obs}) values determined from (**A**, **B**, **E** and **F**) and inhibitor concentration was further investigated in (**C**, **D**, **G** and **H**) and data was subsequently fitted to **Equation 3a** to calculate the forward (k_3) and reverse (k_4) isomerization constants via non-linear regression analysis. Goodness of fits (R^2) for (**C**, **D**, **G** and **H**) were determined to be 0.984, 0.984, 0.986 and 0.996 respectively. Each point in the semi-logarithmic plots represents the mean ± S.D. of triplicate determinations.

Figure 3. Reversible inhibition of CYP17A1 by abiraterone and D4A. Concentration-response plots represent the initial inhibited state (EI) of the CYP17A1-mediated 17α-hydroxylase and C17,20-lyase enzymatic reactions when slow, tight binding inhibitors (**A** and **B**) abiraterone and (**E** and **F**) D4A were introduced. The measured initial velocities (v_i) were used together with velocity of the uninhibited reaction (v_0) to calculate the fractional velocities across various concentrations of abiraterone and D4A (1-300 nM). Using **Equation 2**, apparent dissociation constants (K_i, app) for the initial CYP17A1-inhibitor encounter complexes were first obtained from the midpoint of isotherm curves. K_i, app values were subsequently utilized in non-linear regression analyses (**Equation 3a**) to determine the forward (k_3) and reverse (k_4) isomerization constants. Reversible inhibition experiments were also performed in the presence of multiple substrate (progesterone or 17α-hydroxypregnenolone) and (**C** and **D**) abiraterone or (**G** and **H**) D4A concentrations. To discern the mode of inhibition, Michaelis-Menten plots generated were subjected to double reciprocal transformations to yield Lineweaver Burk graphs as presented in **Supplemental Figure S4**. Based on the identified mode of inhibition, the inhibition

constant for the initial EI complex (K_i) could eventually be derived from K_i, app. Each point represents the mean ± S.D. of triplicate determinations.

Figure 4. Molecular dynamic (MD) simulations investigating the binding of abiraterone to CYP17A1. (**A**) Potential mean force (PMF) profile for the unbinding of abiraterone from CYP17A1. (**B**) Long, unrestrained MD simulations demonstrated two dominant binding modes of abiraterone in CYP17A1 catalytic site. In **Pose A**, the plane of the steroid moiety is near perpendicular to the plane of the heme. (**C**) In **Pose B**, abiraterone is parallel to the plane of the heme. The key-binding region of the CYP17A1 active site is shown in magenta. The side-chain atoms of important binding residues are shown as sticks, abiraterone as thick sticks, and heme as ball and sticks. C, O, and N atoms are shown in cyan, red, and blue, respectively.

Figure 5. VCaP cell-based washout experiments to assess the phenotypic consequence of CYP17A1 engagement following inhibitor removal. (**A**) DHEA formation at increasing concentrations of 17α-hydroxypregnenolone conformed to saturable Michaelis-Menten kinetics (R^2 = 0.974) (**B**) The effect of either abiraterone (20 μM) or ketoconazole (25 μM) co-incubation on 17α-hydroxypregnenolone-mediated dehydroepiandrosterone (DHEA) formation in VCaP cells. Cells were incubated for 2 h at 37°C. (**C**) Time-dependent reversal of CYP17A1 inhibition by abiraterone or ketoconazole as quantified via restoration of DHEA production. VCaP cells were preincubated for 2 h without (control) or with abiraterone (40 μM) or ketoconazole (40 μM), washed, and further incubated with fresh medium for the indicated washout periods before final incubation with 30 μM 17α-hydroxypregnenolone for 30 min. DHEA oxime formation, representing residual CYP17A1 activity in (**B**) and recovery of CYP17A1 activity in (**C**) was expressed as the percentage of maximal DHEA oxime produced in the corresponding vehicle controls. In (**C**), an unpaired t-test revealed overall significant difference between treatment arms across the 60 min washout period (0 min: one-sided p value = 0.0158; 30 min: one-sided p value = 0.0071; 60 min: one-sided p value = 0.0281). Data in (**A**) represent the mean ± S.D. from two experiments with triplicate determinations while data in (**B** and **C**) represent the mean ± S.D. from at least three experiments with triplicate determinations. *p < 0.05; **p < 0.01

Figure 6. Mechanistic pharmacokinetic-pharmacodynamic simulations integrating abiraterone PK and CYP17A1-abiraterone binding kinetics into eventual predictions of efficacy outcomes. (**A**) Simulated apparent CYP17A1 occupancy over time plots after a single *in vivo* dose of 1000 mg or 500 mg of

abiraterone acetate (AA). The clinical plasma concentration-time profiles of abiraterone are represented by open symbols while the solid and dashed lines indicate the predicted percentage apparent CYP17A1 occupancy over time. Time-dependent changes in apparent CYP17A1 engagement were subsequently utilized to predict potential perturbations in the intracellular concentrations of (**B**) dehydroepiandrosterone-sulphate following multiple dose administration of 1000 mg or 500 mg AA over 72 h.

Figure 7. Investigating potential correlations between abiraterone drug levels and the extent of dehydroepiandrosterone-sulphate (DHEA-S) suppression. Results from the Phase II study by Szmulewitz *et al* demonstrated how (**A**) the area under the plasma concentration-time curve of abiraterone from 0-4 h ($AUC_{0\text{-}4h}$), and (**B**) peak plasma concentrations (C_{max}) remained significantly higher in the standard dose arm (1,000 mg abiraterone acetate - AA fasting, n = 20) compared to the low dose arm (250 mg AA, fed, n = 20) (two-sided p value for $AUC_{0\text{-}4h}$ = 0.0417 and two-sided p value for C_{max} = 0.0474). Combined analyses of Phase I trials (Attard *et al* and O' Donnell *et al*, n= 10) in (**A**) and (**B**) revealed that administration of 500 mg of AA in a fasted state yielded AUC values that were greater than that measured in the low dose arm (two-sided p value = 0.0038) whereas C_{max} measurements were not significantly different. AUC and C_{max} data were log transformed and groups comparisons were performed using repeated-measures one-way ANOVA and Dunnett's multiple comparisons tests.

Table 1. *Summary of kinetic constants and dissociation $t_{1/2}$ for the inhibition of CYP17A1 by abiraterone and D4A*

Inhibitor	CYP17A1 Activity	$K_{i,app}$ (nM)[a]	k_3[b] (min^{-1})	k_4[b] (min^{-1})	K_i[c] (nM)	K_i^* (nM)	Dissociation $t_{1/2}$ (h)
Abiraterone	17α-Hydroxylase	132 ± 2.02	0.0353	0.000275	50.7	0.39	42.0
	C17,20-Lyase	118 ± 1.13	0.0224	0.000384	24.8	0.42	30.1
D4A	17α-Hydroxylase	76 ± 1.21	0.0218	0.000396	23.5	0.42	29.2
	C17,20-Lyase	163 ± 3.02	0.0219	0.000121	57.4	0.32	95.5

[a] From plot of $\frac{v_i}{v_0}$ versus [I]. Data represented as mean ± S.D. of triplicate determinations.

[b] From plot of k_{obs} versus [I].

[c] Value of $K_{i,app}$ corrected for mixed mode inhibition.

JPET Fast Forward. Published on June 17, 2020 as DOI: 10.1124/jpet.120.265868
This article has not been copyedited and formatted. The final version may differ from this version.

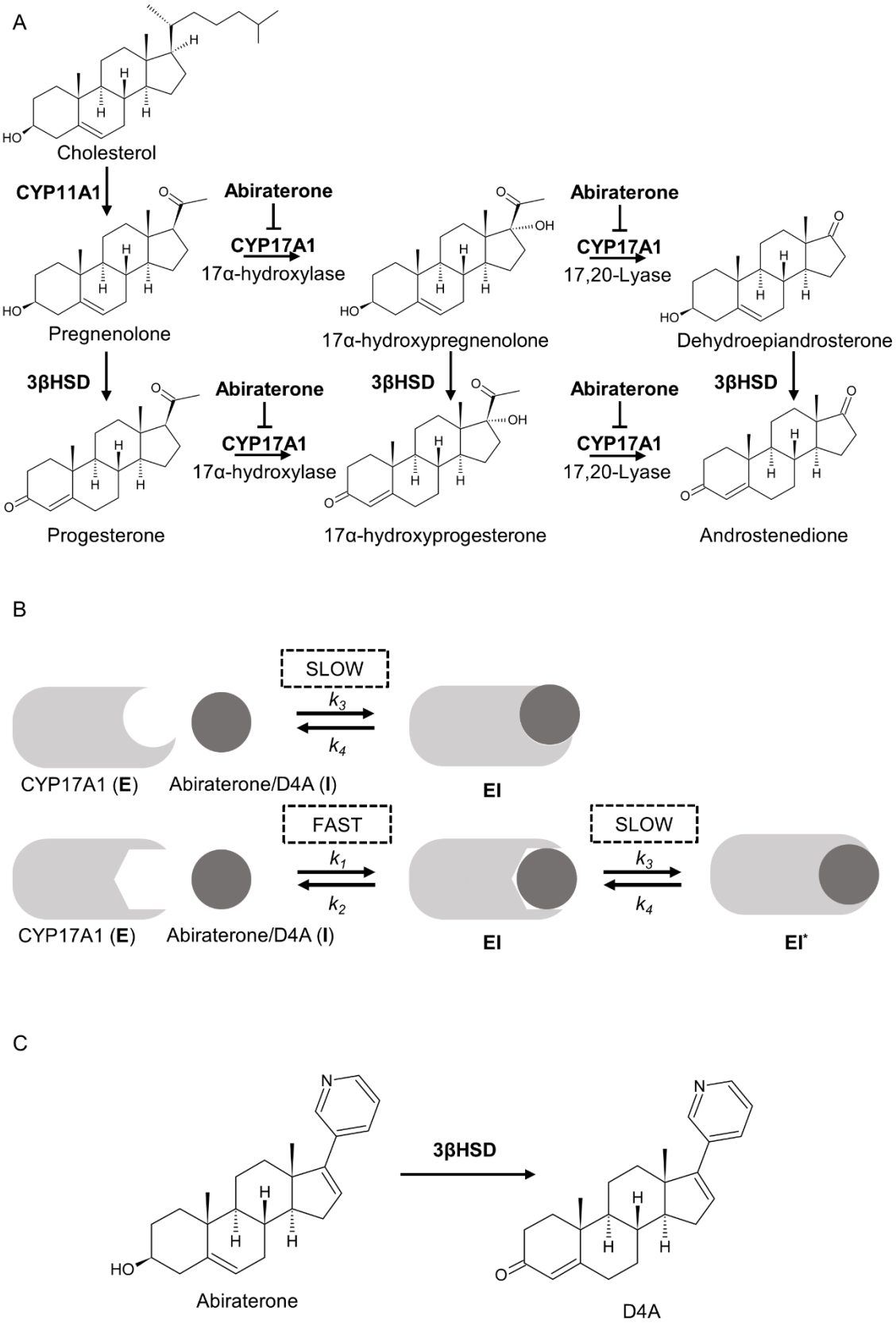

Figure 1

JPET Fast Forward. Published on June 17, 2020 as DOI: 10.1124/jpet.120.265868
This article has not been copyedited and formatted. The final version may differ from this version.

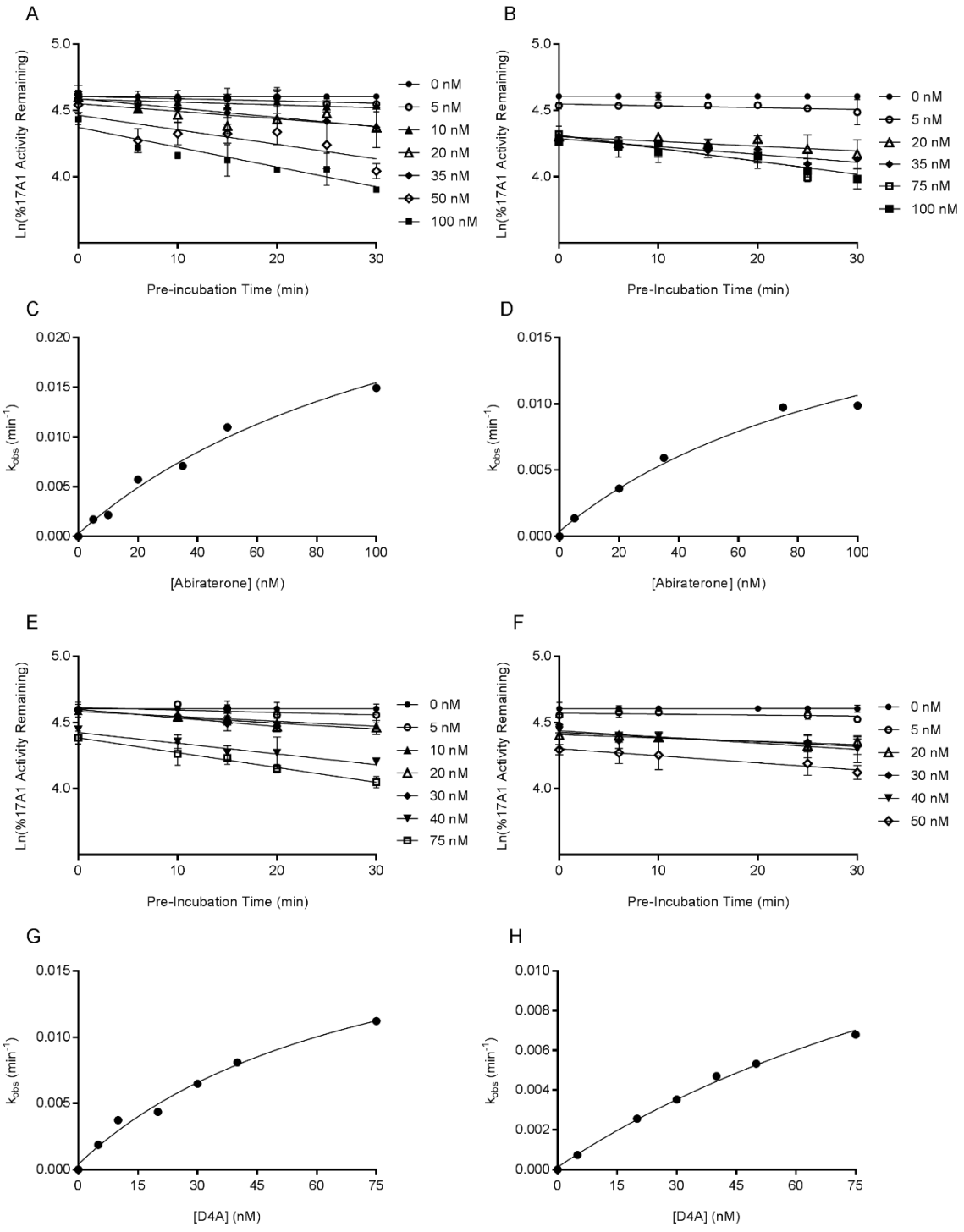

Figure 2

JPET Fast Forward. Published on June 17, 2020 as DOI: 10.1124/jpet.120.265868
This article has not been copyedited and formatted. The final version may differ from this version.

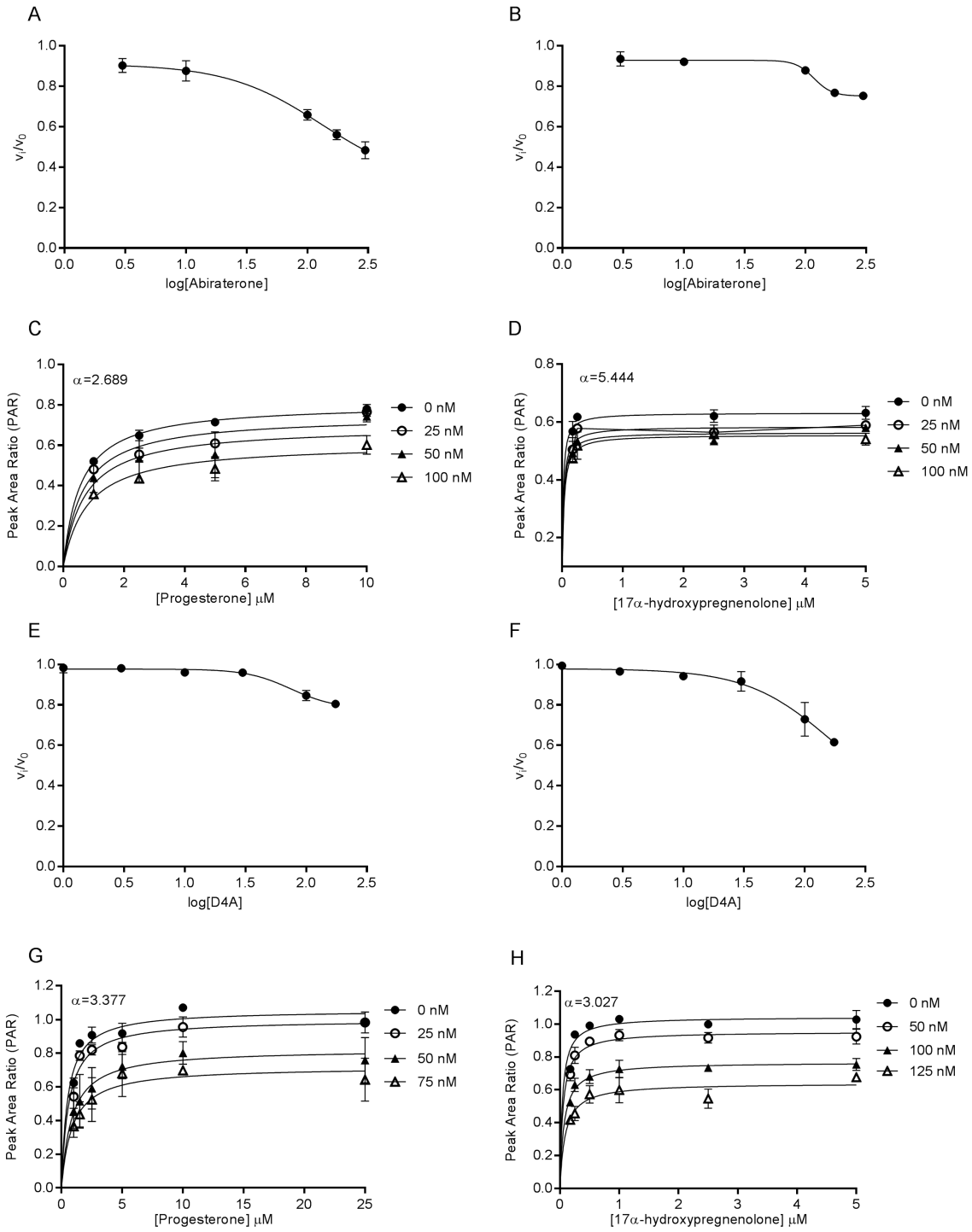

Figure 3

JPET Fast Forward. Published on June 17, 2020 as DOI: 10.1124/jpet.120.265868
This article has not been copyedited and formatted. The final version may differ from this version.

A

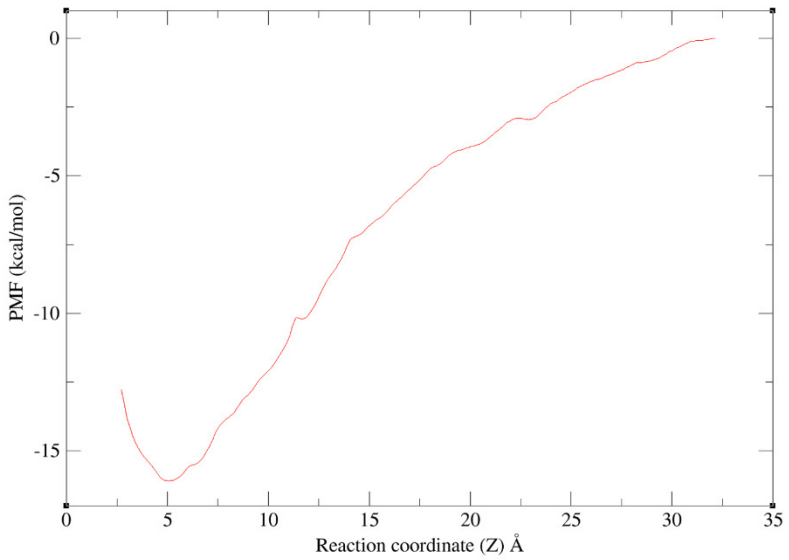

B

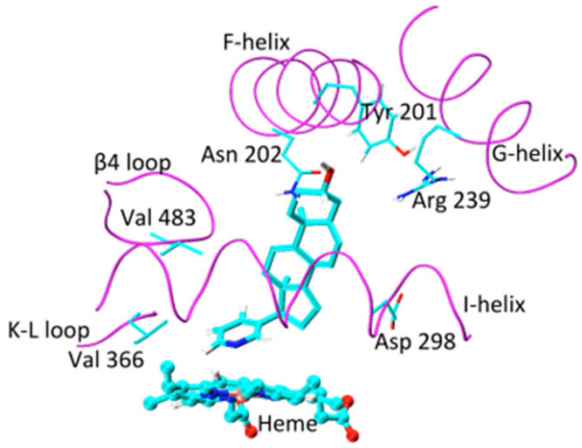

C

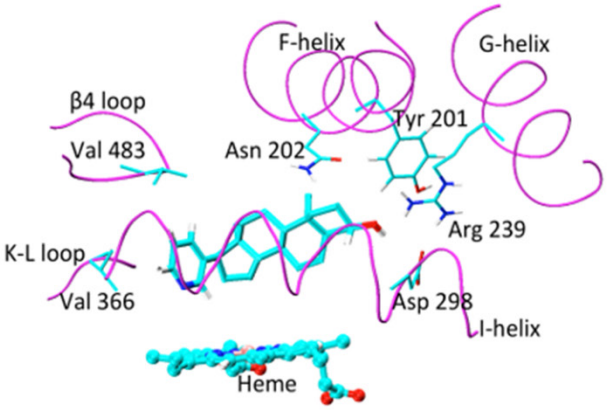

Figure 4

JPET Fast Forward. Published on June 17, 2020 as DOI: 10.1124/jpet.120.265868
This article has not been copyedited and formatted. The final version may differ from this version.

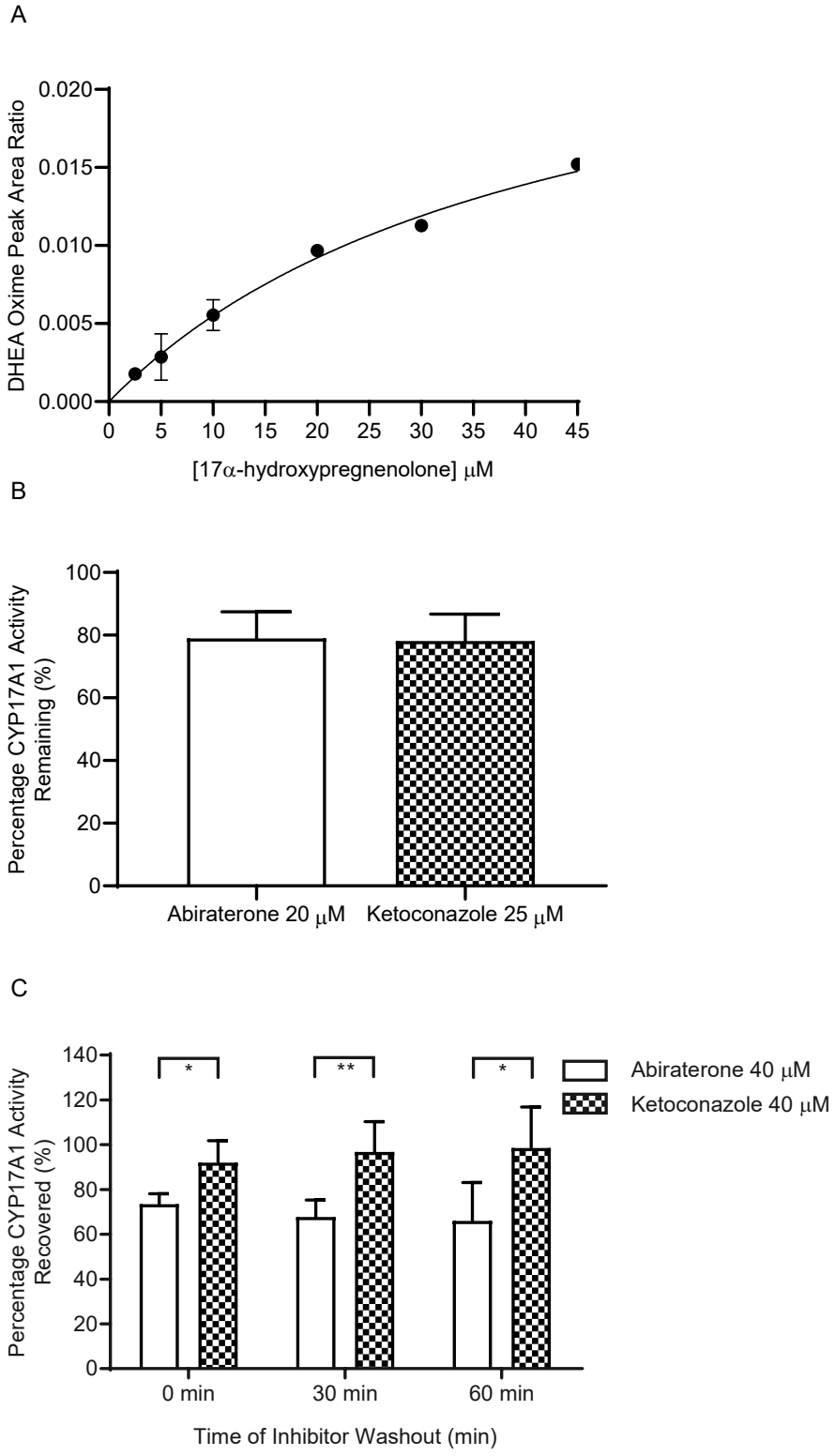

Figure 5

JPET Fast Forward. Published on June 17, 2020 as DOI: 10.1124/jpet.120.265868
This article has not been copyedited and formatted. The final version may differ from this version.

A

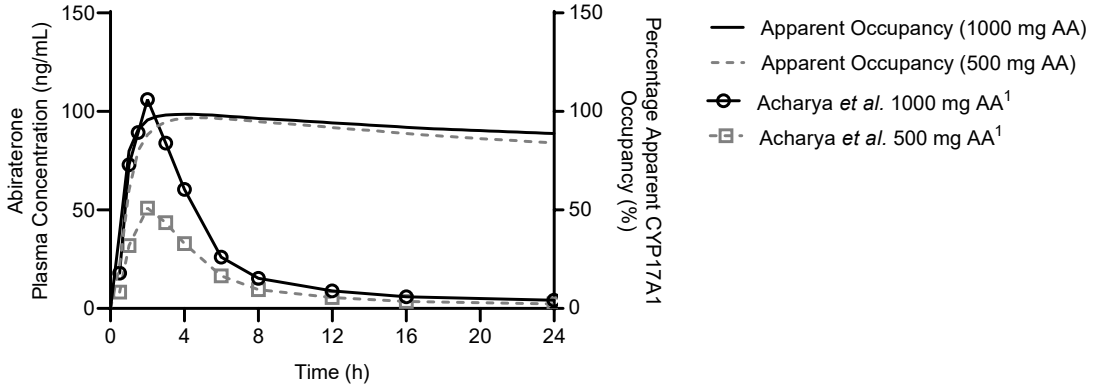

B

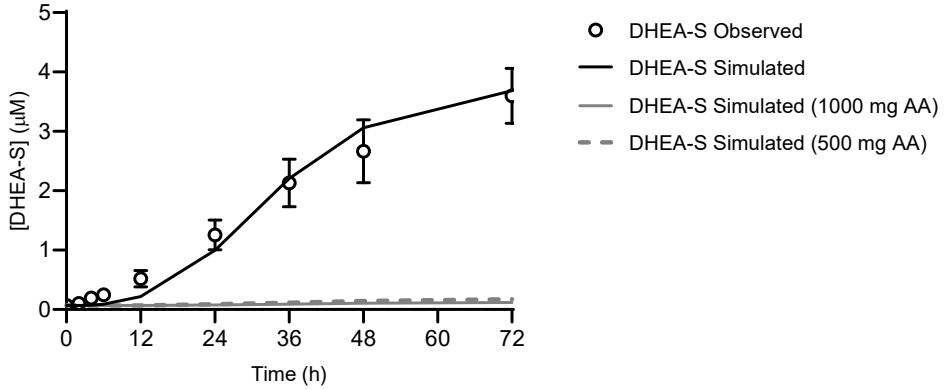

Figure 6

JPET Fast Forward. Published on June 17, 2020 as DOI: 10.1124/jpet.120.265868
This article has not been copyedited and formatted. The final version may differ from this version.

A

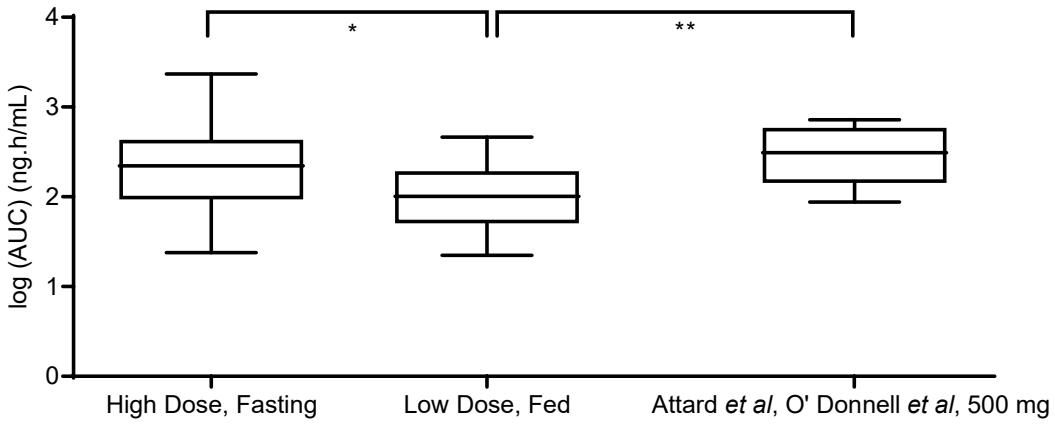

B

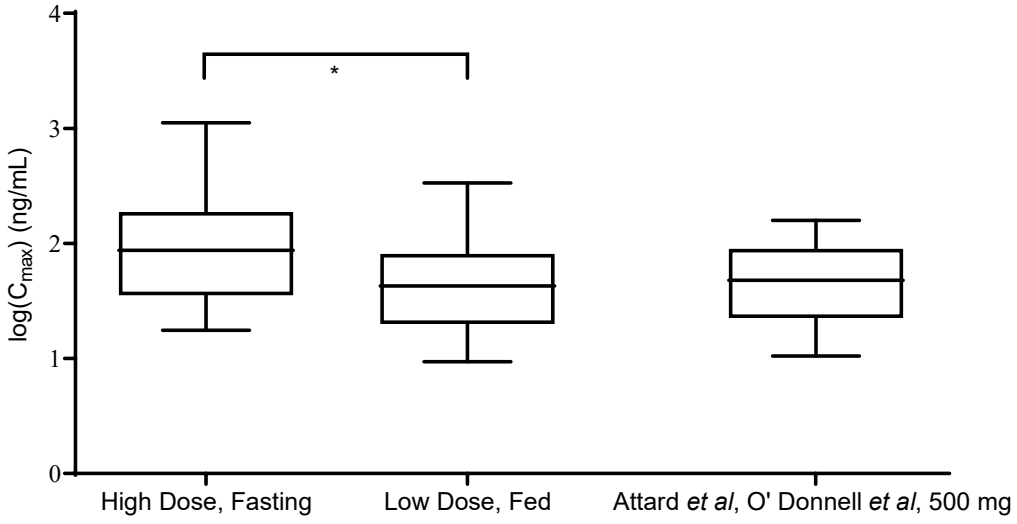

Figure 7

Supplemental Data:

Slow tight binding inhibition of CYP17A1 by abiraterone redefines its kinetic selectivity and dosing regimen

Eleanor Jing Yi Cheong[1], Pramod C Nair[2], Rebecca Wan Yi Neo[1], Ho Thanh Tu[1], Fu Lin[3], Edmund Chiong[4,5], Kesavan Esuvaranathan[4,5], Hao Fan[6], Russell Z. Szmulewitz[7], Cody J. Peer[8], William D. Figg[8], Christina Li Lin Chai[1], John O Miners[2], Eric Chun Yong Chan[1,9]

[1]Department of Pharmacy, Faculty of Science, National University of Singapore, 18 Science Drive 4, Singapore 117543, Singapore; [2]Department of Clinical Pharmacology and Flinders Centre for Innovation in Cancer, College of Medicine and Public Health, Flinders University, Adelaide, Australia; [3]Bioinformatics Institute, Biotransformation Innovation Platform (BioTrans), Agency for Science, Technology and Research (A*STAR), 30 Biopolis Street, Singapore 138671; [4]Department of Surgery, National University Health System, 5 Lower Kent Ridge Road, Singapore 119074, Singapore; [5]Department of Urology, National University Hospital, 5 Lower Kent Ridge Road, Singapore 119074; [6]Bioinformatics Institute, Agency for Science, Technology and Research (A*STAR), 30 Biopolis Street, Singapore 138671; Department of Biological Sciences, National University of Singapore, 14 Science 23 Drive 4, Singapore 117543; Centre for Computational Biology, DUKE-NUS Medical School, 8 College Road, Singapore 169857; [7] The University of Chicago, Chicago, [8]National Cancer Institute, Rockville, MD, [9]National University Cancer Institute, Singapore (NCIS), NUH Medical Centre (NUHMC), 5 Lower Kent Ridge Road, Singapore 119074

1. *Supplemental Methods*

Synthesis of D4A. All reagents and solvents required for synthesis were purchased from commercially available sources (Sigma Aldrich, Alfa Aesar, Tokyo Chemical Industry and Fisher Scientific) and used without purification unless otherwise indicated. Thin layer chromatography (TLC) was performed on Merck silica gel TLC plates with F_{254} fluorescent indicator. Visualization was accomplished with UV light or by staining with $KMnO_4$ solution. Compounds were purified by flash chromatography using Merck silica gel 60 (230–400 mesh. NMR spectra were recorded on a Bruker Avance III 400 MHz spectrometer using chloroform-d (δ 7.26 for 1H NMR, δ 77.16 for 13C NMR) as a solvent. The following abbreviations are used to describe the signals: s = singlet, d = doublet, dd = doublet of doublet, dt = doublet of triplet, t = triplet, m = multiplet, br = broad. The following section details the steps underlying the synthetic scheme presented in **Supplemental Figure S1A**.

Dehydroepiandrosterone acetate (2):

To a solution of dehydroepiandrosterone **(1)** (5.00 g, 17.34 mmol) in pyridine (90 mL) was added Ac_2O (6.56 mL, 69.36 mmol) and DMAP (21 mg, 0.173 mmol). The solution was stirred for 18 hours, following which the mixture was concentrated. The residue was diluted with EtOAc (300 mL), washed several times with HCl 2 M until the aqueous layer remained acidic. The organic layer was dried with Na_2SO_4, filtered and evaporated to give the desired product as a white solid, which was used without purification (5.60 g, 98%).

Spectral data are in agreement with literature values (Li *et al.*, 2016).

^{1}H NMR (400 MHz, $CDCl_3$): δ 5.41 (d, 1H), 4.61 (m, 1H), 2.50-2.28 (m, 3H), 2.16-2.06 (m, 2H), 2.03 (s, 3H), 1.99-1.81 (m, 4H), 1.71-1.43 (m, 6H), 1.33-1.24 (m, 2H), 1.21-1.09 (m, 1H), 1.08-0.99 (m, 4H), 0.92-0.83 (s, 3H).

3β-Acetoxyandrosta-5,16-dien-17-yl trifluoromethanesulfonate (3):

To a solution of **2** (5.10 g, 15.43 mmol) in THF (30 mL) under N_2 at -78°C was added dropwise KHMDS 1M/THF (18.5 mL, 18.52 mmol). The solution was stirred for 30 minutes, then $PhNTf_2$ (6.6 g, 18.52 mmmol) in THF (30 mL) was added dropwise. The solution was stirred for 8 hours, then warmed gradually to RT and quenched with saturated NH_4Cl. The aqueous phase was extracted with EtOAc (3

x 50 mL), then the combined organic layer was washed with brine, dried with Na_2SO_4, filtered and evaporated. Purification by flash chromatography (EtOAc/Pet. Ether 0:100 – 2:98) afforded the desired product as a white solid (5.00 g, 70%).

Spectral data are in agreement with literature values (Li *et al.*, 2016).

^{1}H NMR (400 MHz, $CDCl_3$): δ 5.58 (dd, 1H), 5.39 (m, 1H), 4.60 (m, 1H), 2.38-2.17 (m, 3H), 2.07-1.94 (m, 5H), 1.91-1.55 (m, 8H), 1.52-1.41 (m, 2H), 1.29-1.07 (m, 2H), 1.05 (s, 3H), 0.99 (s, 3H).

Abiraterone acetate (4):

A solution of **3** (3.00 g, 8.64 mmol), 3-(diethylboryl)pyridine (1.91 g, 12.97 mmol), $Pd(PPh_3)Cl_2$ (302 mg, 0.43 mmol) in THF (40 mL) and aqueous Na_2CO_3 2 M (16 mL) was degassed for 5 min. The solution was then refluxed for 1 hour. The cloudy mixture was filtered through Celite, and the filter cake was washed with water (40 mL) and ether (40 mL). The phases were separated, and the aqueous phase was extracted with ether (3 x 30 mL). The combined organic layer was dried with Na_2SO_4, filtered and evaporated. Purification by flash chromatography (EtOAc/Pet. Ether 20:80 – 30:70) afforded the desired product as a white solid (3.20 g, 95%).

Spectral data are in agreement with literature values (Li *et al.*, 2016).

^{1}H NMR (400 MHz, $CDCl_3$): δ 8.62 (s, 1H), 8.45 (d, 1H), 7.64 (dt, 1H), 7.23 (dd, 1H), 5.99 (dd, 1H), 5.43 (d, 1H), 4.62 (m, 1H), 2.45-2.21 (m, 3H), 2.11-1.99 (m, 5H), 1.93-1.61 (m, 8H), 1.55-1.44 (m, 2H), 1.27-1.10 (m, 2H), 1.08 (s, 3H), 1.05 (s, 3H).

Abiraterone (5):

The acetate **4** (350 mg, 0.89 mmol), LiOH (43 mg, 1.79 mmol) was dissolved in THF/H_2O/MeOH 3:1:1 (10 mL). The mixture was stirred for 1 h. The mixture was quenched with saturated NH_4Cl, and the precipitate filtered, washed with water and dried under vacuum to yield the first crop of crude product. The filtrate was extracted with CH_2Cl_2 (5 x 10 mL), then the combined organic layer was dried with Na_2SO_4, filtered and evaporated to yield the second crop of crude product. Purification by flash chromatography (MeOH/ CH_2Cl_2 1:99 – 5:95) afforded the desired product as a white solid (300 mg, 96%).

Purity: 99% (HPLC). Melting point: 225-226 °C (lit. 228-229 °C) (Potter *et al.*, 1995).

Spectral data are in agreement with literature values (Potter *et al.*, 1995; Li *et al.*, 2016).

^{1}H NMR (400 MHz, $CDCl_3$): δ 8.62 (s, 1H), 8.45 (d, 1H), 7.64 (dt, 1H), 7.22 (dd, 1H), 5.99 (dd, 1H), 5.40 (m, 1H), 3.52 (br, 1H), 2.37-2.19 (m, 3H), 2.12-1.95 (m, 3H), 1.89-1.59 (m, 6H), 1.54-1.41 (m, 2H), 1.37-1.20 (m, 4H), 1.07 (s, 3H), 1.05 (s, 3H).

^{13}C NMR (100 MHz, CDCl3): δ 151.43, 146.94, 146.85, 141.36, 134.73, 133.59, 130.08, 123.51, 121.35, 71.74, 57.69, 50.48, 47.49, 42.44, 37.32, 36.83, 35.37, 31.98, 31.76, 31.63, 30.57, 20.98, 19.46, 16.70.

Δ^4-abiraterone (D4A) (6):

A solution of **5** (350 mg, 1.00 mmol) in toluene (25 mL) and cyclohexanone (5 mL) was azeotropically distilled with a Dean-Stark trap until approximately 6 mL of condensate has been collected. The solution was slightly cooled down below reflux temperature, then $Al(iPrO)_3$ (408 mg, 2.00 mmol) was added. The resulting solution was refluxed for 2 h, then cooled to RT and quenched with NaOH 1M (30 mL). The phases were separated, and the aqueous phase was extracted with CH_2Cl_2 (3 x 10 mL). The combined organic layer was dried with Na_2SO_4, filtered and evaporated. Purification by flash chromatography (MeOH/ CH_2Cl_2 1:99 – 5:95) afforded the desired product as a brownish white solid (320 mg, 90%).

Purity: 97% (HPLC). Melting point: 143-145°C (lit. 148-150°C) (Potter *et al.*, 1995).

Spectral data are in agreement with literature values (Potter *et al.*, 1995; Li *et al.*, 2016).

^{1}H NMR (400 MHz, $CDCl_3$): δ 8.61 (s, 1H), 8.47 (s, 1H), 7.63 (dt, 1H), 7.22 (dd, 1H), 5.99 (dd, 1H), 5.76 (s, 1H), 2.54-2.20 (m, 5H), 2.14-1.99 (m, 3H), 1.95-1.61 (m, 6H), 1.52-1.28 (m, 3H), 1.24 (s, 3H), 1.07 (s, 3H).

^{13}C NMR (100 MHz, $CDCl_3$): δ 199.47, 170.81, 150.74, 145.54, 145.42, 136.03, 134.03, 130.92, 124.24, 124.08, 56.94, 54.02, 47.52, 38.82, 35.73, 35.16, 34.23, 34.06, 32.85, 31.90, 31.86, 21.00, 17.38, 16.75.

Upon synthesis, the purity of D4A was ascertained by analytical HPLC with a Phenomenex Kinetex 2.6 mm C_{18}-100 (150 x 4.60 mm) column at 254 nm (**Supplemental Figure S1B**).

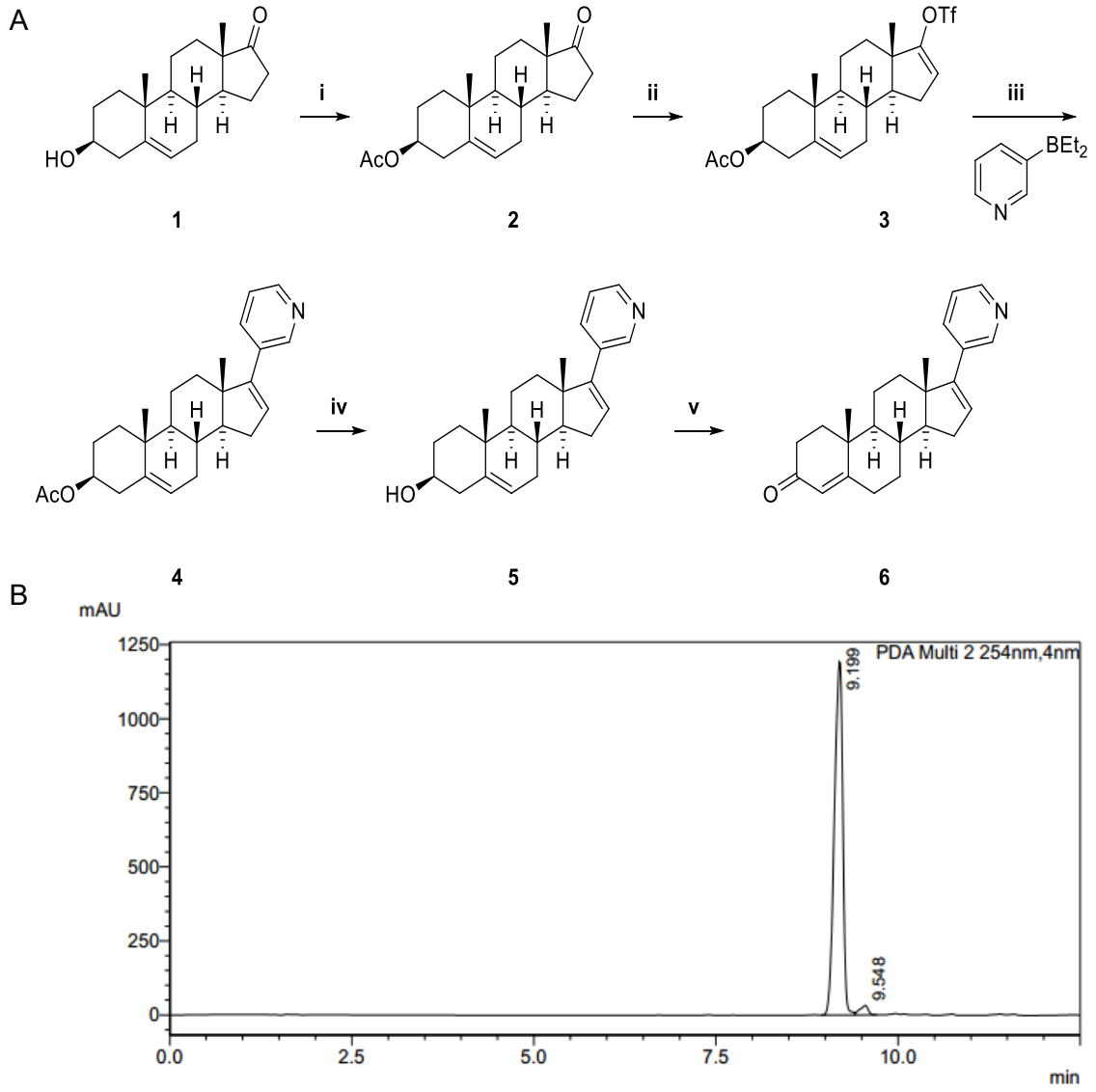

Supplemental Figure S1. Synthesis and characterization of D4A. (**A**) Synthetic scheme leading to the production of D4A. Reagents required in each of the 6 steps are follows: Reagents: i) Ac_2O, DMAP, pyridine, 98%; ii) KHMDS, $PhNTf_2$, THF, -78˚C, 70%; iii) $Pd(PPh_3)_2Cl_2$, Na_2CO_3, THF, H_2O, reflux, 95%; iv) LiOH, THF, H_2O, MeOH, 96%; v) $Al(iPrO)_3$, toluene, cyclohexanone, reflux, 90%. (**B**) HPLC chromatogram of synthesized D4A.

Preliminary Optimization of Pre-incubation Time-Dependent Assays. High substrate concentrations relative to the Michaelis constant (K_m), otherwise defined as concentration of substrate that produces half-maximal enzyme velocity, were utilized to ensure that substrate depletion did not contribute to any observed loss in rCYP17A1 activity. The saturating substrate conditions ($\frac{K_m}{[S]} \ll 1$) also raised the resultant inhibitor concentration $[I]$ required to cause inhibition to levels significantly higher than the enzyme concentration $[E]$, hence circumventing putative tight binding behavior that occurs when $[E] \approx [I]$ (Morrison, 1982). To determine the K_m for both progesterone 17α-hydroxylation and 17α-hydroxypregnenolone C17,20-lyase reactions, metabolite formation was monitored as a surrogate for reaction velocity and plotted against substrate concentration. However, as shown in **Supplemental Figures S2A** and **B**, substrate-velocity curves appeared sigmoidal, suggesting deviation from hyperbolic kinetics and the presence of positive cooperativity (Copeland, 2004). Hence, the influence of cooperativity on the measured values of velocity was evaluated via **Equation S1** (Copeland, 2004)**,** where K' is related to K_m, but also contains terms describing the effect of substrate occupancy at one site on the substrate affinity of other sites. The degree of cooperativity was quantified by the Hill coefficient, h.

$$v = \frac{V_{max} \times [S]^h}{K' + [S]^h} \qquad \textbf{[S1]}$$

In the presence of saturating substrate concentrations (K'/[S]<< 1), product formation of the uninhibited reaction was observed to remain linear over the incubation time of 20 min (**Supplemental Figures S2C** and **D**).

Oxime Derivatization of DHEA and Androstenedione. For the C17,20-lyase pathway, oxime derivatization of DHEA and androstenedione (internal standard) was performed to improve the ionization efficiency and thus increase analytical sensitivity during final liquid chromatography tandem mass spectrometry (LC/MS/MS) analysis (**Supplemental Figure S3**) (Keski-Rahkonen *et al.*, 2011; Ming *et al.*, 2014). 70 µL of 100 mM hydroxylamine hydrochloride solution (50% v/v methanol:water) was added to an equal volume of sample supernatant obtained after protein precipitation and centrifugation. The mixture was heated at 60°C for 1 h to allow derivatization to occur, followed by centrifugation at 4°C and 2755 *g* for 10 min prior to LC/MS/MS analysis (**Supplemental Table S1**).

Determining the Inhibition Modality for Abiraterone/D4A. To determine the mode of inhibition for the initial enzyme-inhibitor encounter (EI) complex, reversible inhibition assays and subsequent Lineweaver-Burk (double-reciprocal) transformations were performed. **Equation S2** was next applied to correct K_i, app to the true dissociation constant K_i, where [S] represents the substrate concentration used in the concentration response analysis of the initial step of enzyme inhibition, K' is the concentration of substrate that produces half-maximal enzyme velocity (**Supplemental Figures S2A** and **B**) and α is the degree to which inhibitor binding in a mixed mode inhibition model alters the affinity of the enzyme for the substrate (Zhang and Wong, 2005).

$$K_i, app = \frac{K_i \times \left(1 + \frac{[S]}{K'}\right)}{1 + \frac{K_i}{\alpha \times K_i} \times \frac{[S]}{K'}} \qquad \textbf{[S2]}$$

Depending on the magnitude of α, **Equation. S2** can incorporate competitive, uncompetitive and noncompetitive inhibition modes as special cases.

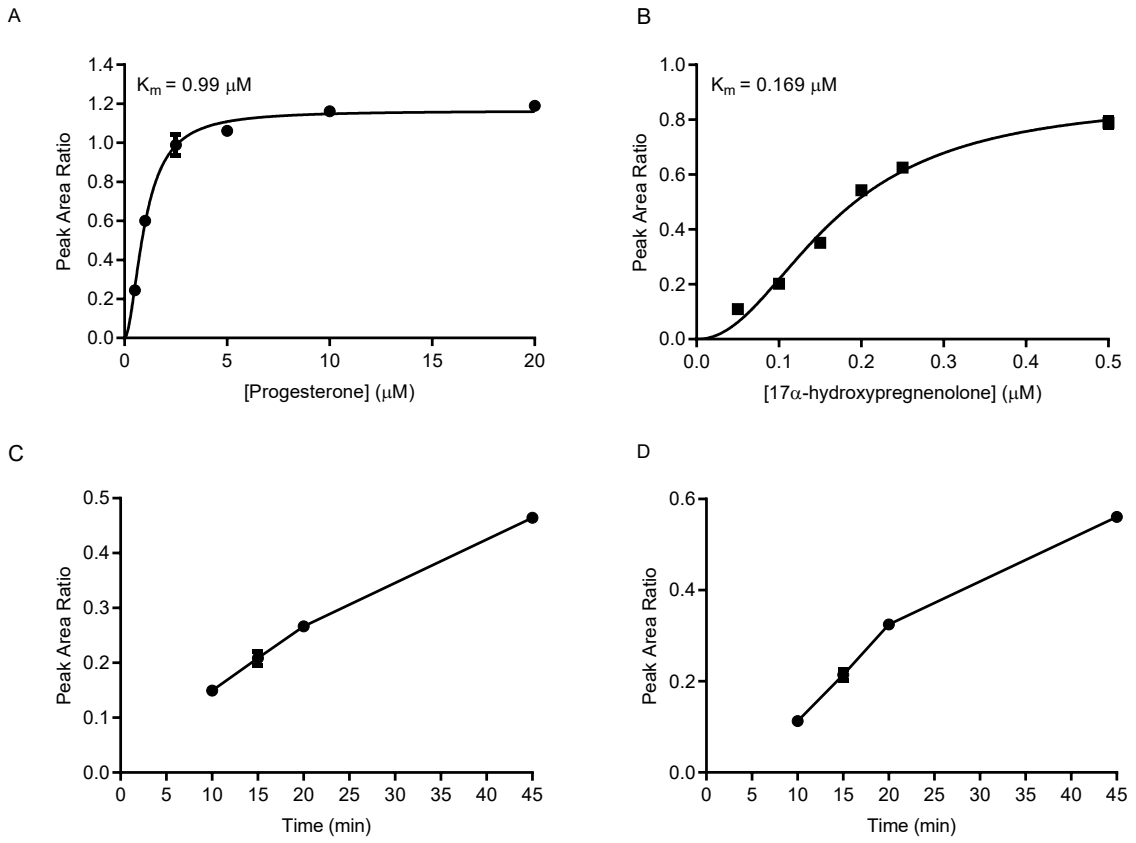

Supplemental Figure S2. Preliminary optimization of enzymatic assay conditions. Plots examining the dependence of reaction velocity on substrate concentration for (**A**) progesterone 17α-hydroxylation and (**B**) 17α-hydroxypregnenolone C17,20-lyase reaction. Data conformed to an allosteric sigmoidal model and K' was determined to be 0.99 and 0.169 μM respectively. (**C**, **D**) In the presence of saturating substrate concentrations (K'/[S]<< 1), product formation remained linear up to 20 min.

A

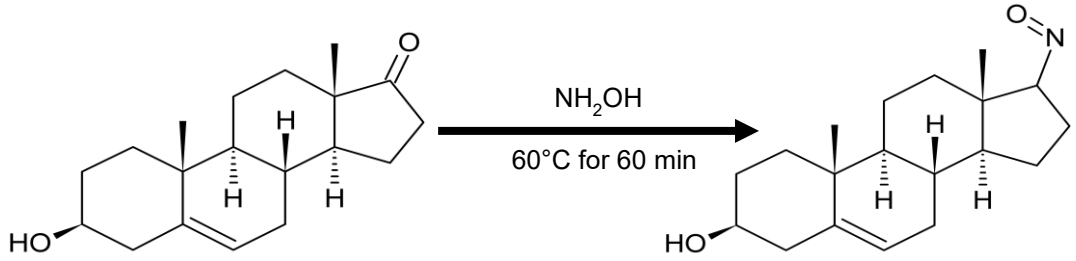

B

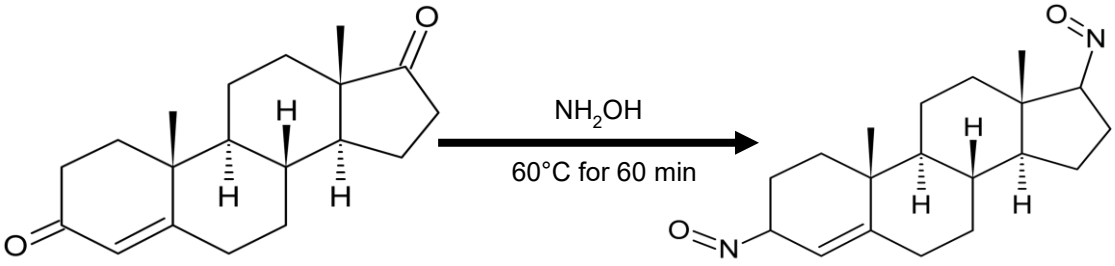

C

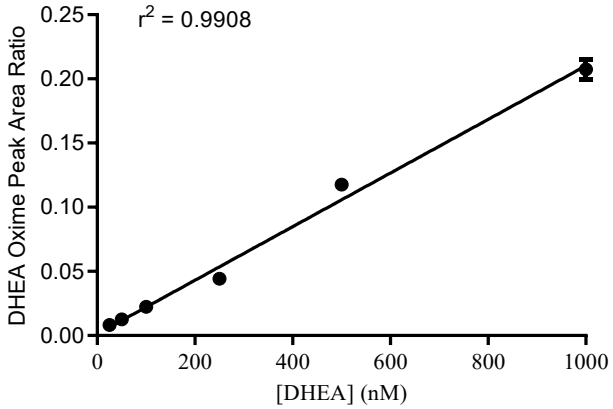

Supplemental Figure S3. Oxime derivatization of DHEA and Androstenedione. Hydroxylamine derivatives of (**A**) DHEA and (**B**) Androstenedione. (**C**) Linearity was observed in the calibration curve constructed using 25, 50, 100, 250, 500 and 1000 nM of DHEA after derivatization, implying that the peak area ratio (PAR) of DHEA oxime and androstenedione oxime could be used as a proxy for DHEA formation.

Liquid-Liquid Extraction for LC/MS/MS Analysis of Culture Media Samples. Collected media samples were spiked with 2.02 µL of 1 µg/mL testosterone-2,3,4-$^{13}C_3$ and subjected to a 2-step liquid-liquid extraction (LLE). In the first extraction, 1 mL of methyl tert butyl ether (MTBE) was aliquoted into each tube and vortexed at high speed for 5 min. Samples were then centrifuged using a microfuge at 18 000 *g* for 5 min at 4°C to ensure complete separation of the media from the extraction solvent. 800 µL of MTBE was carefully aliquoted from each tube to a corresponding 2 mL Eppendorf tube. For the second extraction, another 800 µL of MTBE was added, vortexed and spun down in a similar manner before 800 µL of MTBE was aliquoted and added to the same corresponding tube. The extraction solvent was then dried down in a turbovap using nitrogen gas at 3-5 psi before reconstitution in 50 µL of 100 mM hydroxylamine hydrochloride solution (50% v/v methanol:water) and heated at 60°C for 1 h prior to LC/MS/MS measurement of DHEA oxime formation (Ming *et al.*, 2014).

Supplemental Table S1. *Optimized Compound-Specific MS Parameters for LC/MS/MS Analysis*

Analyte	Q1 Mass (Da)	Q3 Mass (Da)	DP (Volts)	EP (Volts)	CE (Volts)	CXP (Volts)
17α-hydroxyprogesterone	331.0	97.0	100	8	27	6
Prednisolone	361.2	343.0	100	6	15	7
DHEA Oxime	304.2	253.1	60	10	17	14
Androstenedione Oxime	317.2	112.0	80	10	30	13
Testosterone-2,3,4-$^{13}C_3$ oxime	307.3	127.1	110	10	37	10

Q1 Mass: Mass of Parent Ion

Q3 Mass: Mass of Daughter Ion with Best Sensitivity

DP: Declustering Potential

EP: Entrance Potential

CE: Collision Energy

CXP: Collision Cell Exit Potential

Supplemental Table S2. *Rate constants for simulation of the temporal evolution of target occupancy after a single abiraterone acetate dose*

Rate Constants	Value	Comment
k_1 ($\mu M^{-1}h^{-1}$)	2808	Estimates obtained from Gonzalez *et al* assuming similar association rates between abiraterone and pregnenolone (Gonzalez and Guengerich, 2017) Satisfies the upper limit on the value of k_1 ~10^8-$10^9 M^{-1}s^{-1}$/~6000-60,000 $\mu M^{-1}h^{-1}$ as defined by Copeland *et al.* (Copeland *et al.*, 2006; Copeland, 2016) which represents the rate of diffusion of the two binding partners in physiological solutions
k_2 (h^{-1})	370.66	Satisfies the inequalities and K_i, app specified in ***Modelling of Target Occupancy in the Methods Section*** $k_2 \gg k_3 + k_4 = 2.12 + 0.017 = 2.14\ h^{-1}$ $k_1 \gg \frac{k_4}{K_i^*} = \frac{0.017}{3.9\times10^{-4}} = 43.6\ \mu M^{-1}h^{-1}$ $K_i, app = \frac{k_2}{k_1} = 0.132\ \mu M$
k_3 (h^{-1})	2.12	Derived from pre-incubation time-dependent assays (inhibition of the 17α-hydroxylase pathway by abiraterone)
k_4 (h^{-1})	0.017	Derived from pre-incubation time-dependent assays (inhibition of the 17α-hydroxylase pathway by abiraterone)
k_{syn} ($\mu M.h^{-1}$)	0.82	Derived from the *in vivo* steady state concentration of CYP17A1 (41 μM) given that $[E]_{ss} = \frac{k_{syn}}{k_{deg}}$
k_{deg} (h^{-1})	0.02	Assumed to be equal to the k_{deg} of CYP3A4

k_1 and k_2, forward and reverse microscopic rate constants of the rapid reversible binding of E+I to form EI; k_3 and k_4, forward and reverse microscopic rate constants of the slow subsequent isomerization of EI to form EI*; k_{syn} and k_{deg}, zero order rate of synthesis and first order rate of degradation of CYP17A1 *in vivo*

Modelling the Implications of Time-Dependent Changes in CYP17A1 Occupancy on Intracellular Steroidogenesis. By studying the time course for steroid synthesis over 72 h in H295R cells that were stimulated with forskolin, Eldin *et al* developed a dynamic model of steroidogenesis where first order reaction rates (v) within the network were described by apparent rate constants (k) and the concentrations of the precursor steroids (Substrate = S) (Eldin *et al.*, 2018).

Model Assumption 1: Defining all enzymatic reactions within the steroidogenic pathway via first order equations is governed by the underlying assumption that substrate concentrations are substantially lower than the Michaelis constant ($S \ll K_m$). As such, the Michaelis-Menten rate equation (**Equation S3a**) can be approximated with **Equation S3b**. The reaction rate (v) can alternatively be presented as a negative rate of change in substrate concentration ($v = -\frac{ds}{dt}$). As presented in **Equation S3c**, the apparent rate constant (k) is thus equal to $E_0 \frac{k_{cat}}{K_m}$.

$$v = E_0 k_{cat} \frac{S}{S + K_m} \quad \textbf{[S3a]}$$

$$v \approx E_0 k_{cat} \frac{S_0}{K_m} \quad \textbf{[S3b]}$$

$$\frac{dS}{dt} = -E_0 \frac{k_{cat}}{K_m} \times S \quad \textbf{[S3c]}$$

where E_0 is the enzyme concentration, k_{cat} is the turnover number and K_m is the Michaelis-Menten constant.

Model Assumption 2: Additionally, although enzymatic reactions should involve an intermediate step of ES complex formation, the second assumption made is that the initial phase of complex formation is rapid and that all metabolic reactions are in quasi-equilibrium condition (Mangelis *et al.*, 2016). This “hit and run” symbolic model of enzymatic catalysis is denoted by E + S → E + P, where there is zero overall change in enzyme concentration over time (Schwartz *et al.*, 2014).

To prospectively simulate changes in CYP17A1 concentration upon administration of abiraterone acetate and the subsequent inhibitory effect exerted on the CYP17A1-mediated pregnenolone 17α-hydroxylase and 17α-hydroxypregnenolone C17,20 lyase reactions, we utilized the steroidogenesis model developed by Eldin *et al*., with a few modifications (Eldin *et al.*, 2018). **Equations S4a-f** represent the system of ordinary differential equations that was constructed. Pregnenolone concentrations were first interpolated to provide a time continuous input for initiation of steroidogenesis. To ensure that reaction rates are proportional to $[E] \times [S]$ in the sequential conversion of pregnenolone to 17α-hydroxypregnenolone to DHEA, the apparent rate constants (k_2, k_3) obtained by *Eldin et al.* were corrected for the steady state CYP17A1 concentration (E_0 defined in **Supplemental Table S2** as 41 μM) to obtain $\frac{k_{cat}}{K_m}$ (**Equations S4a-b**). In the absence of an inhibitor (I), **Equation S4d** describes the constant steady state CYP17A1 concentration that will be observed over time upon numerical integration. In the presence of abiraterone acetate administered once daily for 72 h, time-dependent changes in CYP17A1 occupancy were modelled using **Equations 4d to 4f**, where rate constants (k_8, k_9, k_{10}, k_{11}) are analogous to (k_1, k_2, k_3, k_4) defined in **Supplemental Table S2**. CYP17A1 engagement varying as a function of both abiraterone concentration and time will manifest as dynamic changes in CYP17A1 concentration, which will function as input into **Equations S4a-b** for simulation of steroidogenic perturbations.

$$\frac{d[17\alpha\text{−hydroxypregnenolone}]}{dt} = \frac{k_2}{41} \times [E] \times [Pregnenolone]_{input} - \frac{k_3}{41} \times [E] \times [17\alpha - \text{hydroxypregnenolone}] - k_4[17\alpha - \text{hydroxypregnenolone}] \quad \textbf{[S4a]}$$

$$\frac{d[DHEA]}{dt} = \frac{k_3}{41} \times [E] \times [17\alpha - \text{hydroxypregnenolone}] - k_5[DHEA] - k_6[DHEA] \quad \textbf{[S4b]}$$

$$\frac{d[DHEA - S]}{dt} = k_5[DHEA] \quad \textbf{[S4c]}$$

$$\frac{d[E]}{dt} = k_{syn} - k_{deg}[E] + k_9[EI] - k_8[E][I] \quad \textbf{[S4d]}$$

$$\frac{d[EI]}{dt} = k_8[E][I] - k_9[EI] + k_{11}[EI^*] - k_{10}[EI] \quad \textbf{[S4e]}$$

$$\frac{d[EI^*]}{dt} = k_{10}[EI] - k_{11}[EI^*] \quad \textbf{[S4f]}$$

2. Supplemental Results

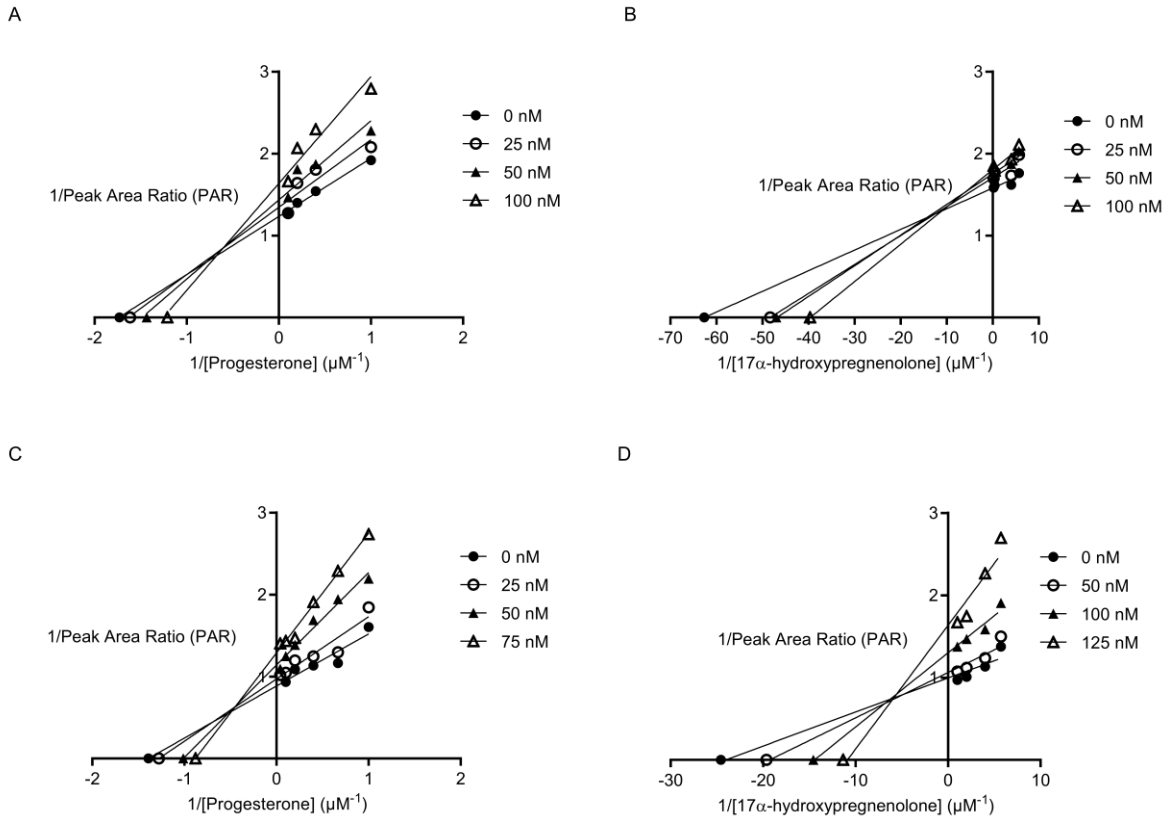

Supplemental Figure S4. Determination of the mode of CYP17A1 Inhibition by abiraterone and D4A. Lineweaver-Burk transformations affirming mixed mode inhibition of CYP17A1-mediated 17α-hydroxylation and C17,20-lyase reactions by (**A** and **B**) abiraterone and (**C** and **D**) D4A.

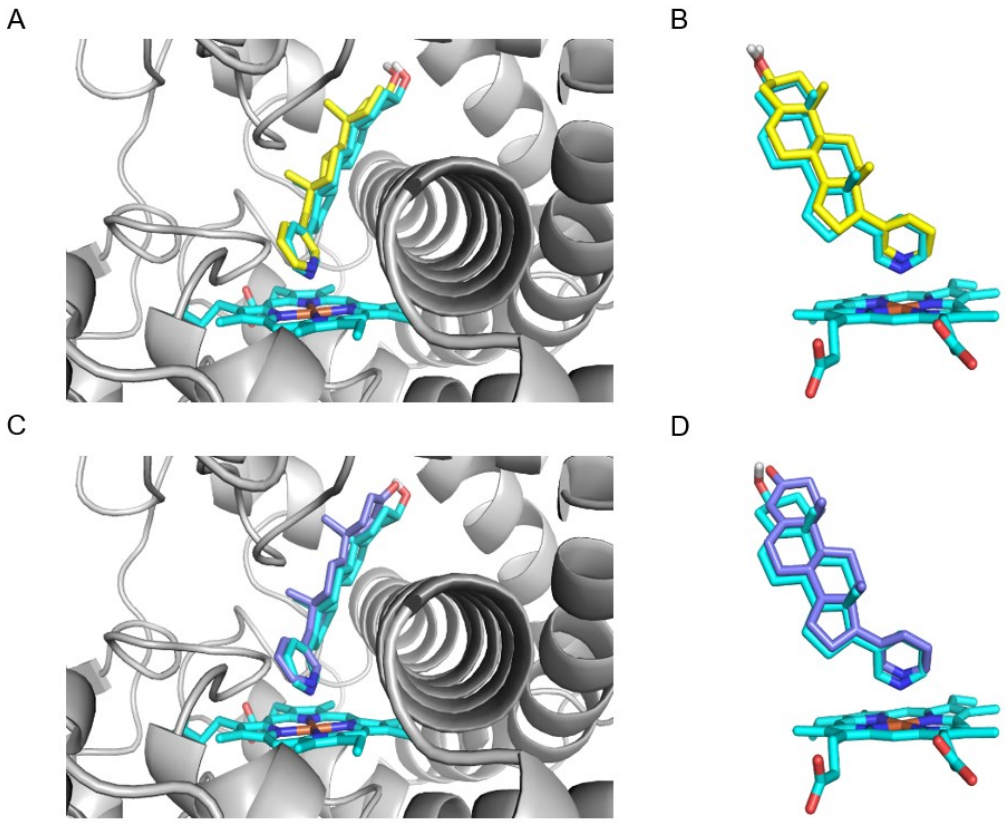

Supplemental Figure S5. Molecular docking of abiraterone/D4A in CYP17A1. The compounds abiraterone and D4A were non-covalently docked to human CYP17A1 with the molecular docking program GOLD, version 2016. Docking poses of abiraterone (**A** and **B**) and D4A (**C** and **D**). CYP17A1 is hidden for clarity in (**B**) and (**D**). The CYP17A1-abiraterone crystal structure is colored in cyan, while the docking poses of abiraterone and D4A are colored in yellow and purple respectively. The docking poses of both abiraterone and D4A compare well with the binding motif of abiraterone in the crystal complex. During docking, several crucial parameters such as the generation of evolution, population size, island number, rate of mutation, and the rate of crossover were systematically explored to achieve the best score in ChemScore. The optimal parameters are listed as follows: population size = 500; island number = 10; generation of evolution = 50000000; mutation rate = 0.5; crossover rate = 0.8.

A

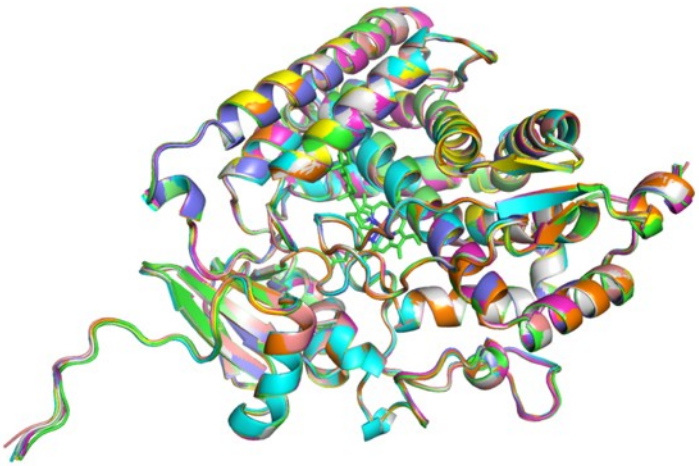

B

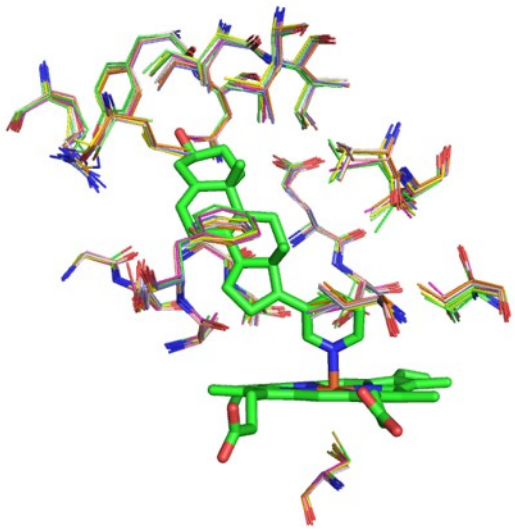

Supplemental Figure S6. Superimposition of 9 available crystal structures for the ligand-bound (holo) CYP17A1 (PDB codes: 3RUK, 3SWZ, 4NKV, 4NKW, 4NKX, 4NKY, 4NKZ, 5IRQ, and 5IRV) demonstrates that (**A**) the overall secondary structures of CYP17A1 are highly ordered while (**B**) the sidechains of binding pocket residues show some degree of flexibility.

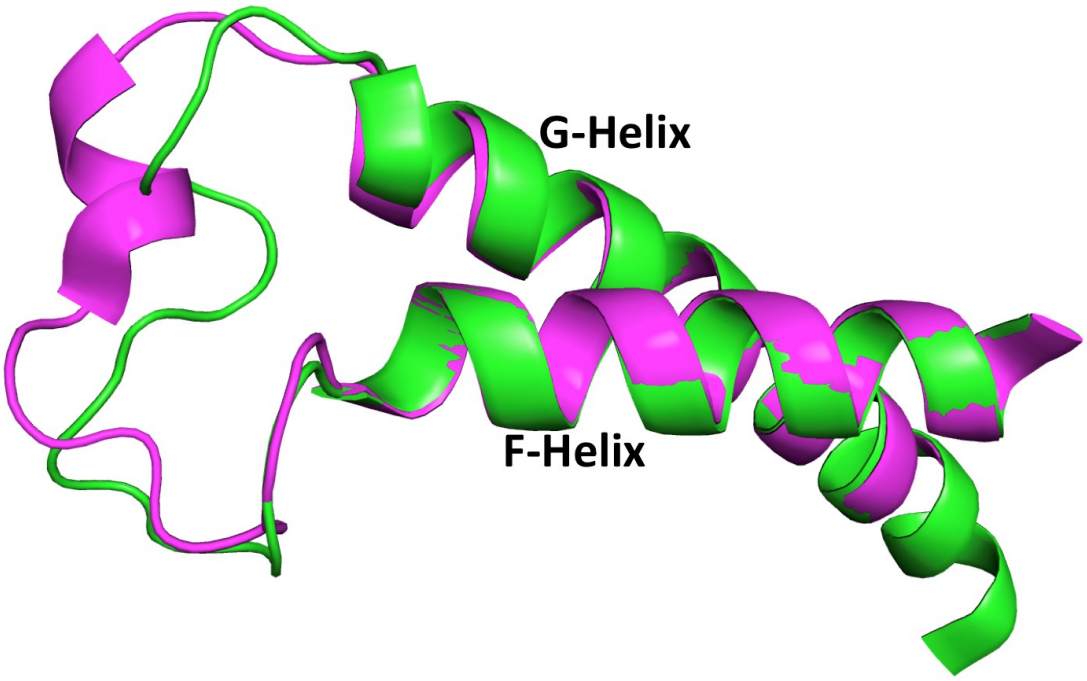

Supplemental Figure S7. The secondary structure of the region connecting the F and G helices in molecules A, B (magenta) and C, D (green) of the X-ray crystal structure 3RUK.

A

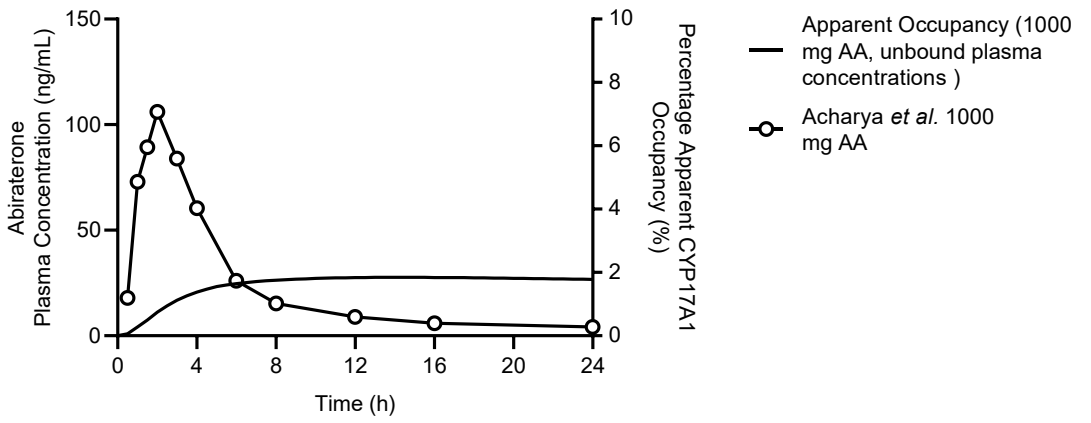

B

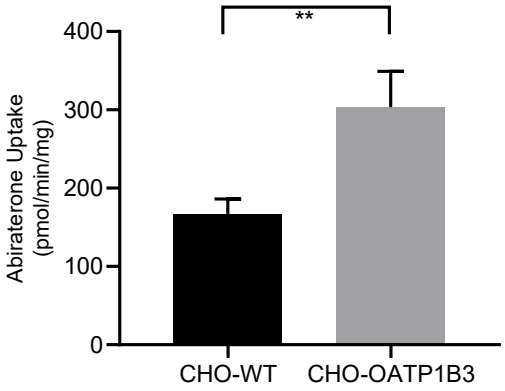

Supplemental Figure S8. Investigation of factors affecting target exposure that might implicate apparent CYP17A1 occupancy (**A**) Rather than using total plasma concentrations as a surrogate for target exposure, the plasma free fraction of abiraterone following a single 1000 mg dose of abiraterone acetate was used. (**B**) Demonstration of organic anion transporting polypeptide (OATP)1B3-mediated uptake of abiraterone (5 μM) suggests that transporter-mediated uptake mechanisms could potentially create and maintain asymmetry between free abiraterone concentrations in plasma and tissue.

Supplemental Table S3. *Root mean square fluctuations (RMSF) of CYP17A1 Cα atoms and side chains located within 8 Å of bound abiraterone.*

	RMSF (Å)		
Amino acid	**Cα atoms**	**Side Chain**	**Location**
102	1.1	1.5	B' helix
105	1.2	1.2	B' helix
106	1.1	1.2	B' helix
112	1.1	1.5	loop between helices B' and C
113	1.0	1.1	loop between helices B' and C
114	1.0	1.4	loop between helices B' and C
197	1.3	1.8	F-helix
198	1.3	1.9	F-helix
199	1.6	2.2	F-helix
200	1.6	1.9	F-helix
201	1.6	2.8	F-helix
202	1.4	1.2	F-helix
203	1.3	2.0	F-helix
204	1.5	-	F-helix
205	1.6	2.0	F-helix
206	1.3	1.8	F-helix
207	1.3	1.9	F-helix
209	1.8	2.5	F-helix
214	1.2	1.5	loop after F helix
232	1.1	1.5	G-helix
235	1.0	1.2	G-helix
236	1.1	1.5	G-helix
239	0.9	1.2	G-helix
243	1.0	1.1	G-helix
294	1.0	1.3	I-helix

295	0.7	1.2	I-helix
296	0.7	1.3	I-helix
297	0.8	-	I-helix
298	0.8	1.3	I-helix
299	0.7	1.1	I-helix
300	0.7	1.4	I-helix
301	0.8	-	I-helix
302	0.8	0.9	I-helix
303	0.8	-	I-helix
304	0.8	1.3	I-helix
305	0.7	1.3	I-helix
306	0.7	0.8	I-helix
307	0.7	0.8	I-helix
365	0.9	1.0	K-L loop
366	1.1	1.8	K-L loop
367	0.9	1.0	K-L loop
368	0.9	1.0	K-L loop
370	1.0	1.5	K-L loop
371	1.0	1.4	K-L loop
434	1.1	1.3	loop preceding L-helix
435	1.5	1.9	loop preceding L-helix
441	1.8	2.7	loop preceding L-helix
442	0.9	1.4	loop preceding L-helix
443	1.0	1.6	loop preceding L-helix
444	1.3	-	loop preceding L-helix
481	1.5	2.0	β4 loop
482	1.4	1.8	β4 loop
483	1.2	1.7	β4 loop
484	1.0	1.8	β4 loop

Supplemental Data References

Copeland RA (2004) *Enzymes: A Practical Introduction to Structure, Mechanism, and Data Analysis*, Wiley.

Copeland RA (2016) The drug-target residence time model: A 10-year retrospective. *Nat Rev Drug Discov* **15**:87–95.

Copeland RA, Pompliano DL, and Meek TD (2006) Drug–target residence time and its implications for lead optimization. *Nat Rev Drug Discov* **5**:730–739.

Eldin K, Ahmed M, Frøysa HG, André O, Sagen J V, Mellgren G, Verhaegen S, Ropstad E, Goksøyr A, and Kellmann R (2018) LC-MS/MS based profiling and dynamic modelling of the steroidogenesis pathway in adrenocarcinoma H295R cells. *Toxicol Vitr* **52**:332–341.

Gonzalez E, and Guengerich FP (2017) Kinetic processivity of the two-step oxidations of progesterone and pregnenolone to androgens by human cytochrome P450 17A1. *J Biol Chem* **292**:13168–13185.

Keski-Rahkonen P, Huhtinen K, Poutanen M, and Auriola S (2011) Fast and sensitive liquid chromatography-mass spectrometry assay for seven androgenic and progestagenic steroids in human serum. *J Steroid Biochem Mol Biol* **127**:396–404.

Li Z, Alyamani M, Li J, Rogacki K, Abazeed M, Upadhyay SK, Balk SP, Taplin M-E, Auchus RJ, and Sharifi N (2016) Redirecting abiraterone metabolism to fine-tune prostate cancer anti-androgen therapy. *Nature* **533**:547–551.

Mangelis A, Dieterich P, Peitzsch M, Richter S, Jühlen R, Hübner A, Willenberg HS, Deussen A, Lenders JWM, and Eisenhofer G (2016) Computational analysis of liquid chromatography-tandem mass spectrometric steroid profiling in NCI H295R cells following angiotensin II, forskolin and abiraterone treatment. *J Steroid Biochem Mol Biol* **155**:67–75.

Ming DS, Pham S, Deb S, Chin MY, Kharmate G, Adomat H, Beheshti EH, Locke J, and Guns ET (2014) Pomegranate extracts impact the androgen biosynthesis pathways in prostate cancer models in vitro and in vivo. *J Steroid Biochem Mol Biol* **143**:19–28.

Morrison JF (1982) The slow-binding and slow, tight-binding inhibition of enzyme-catalysed reactions. *Trends Biochem Sci* **7**:102–105.

Potter GA, Barrie SE, Jarman M, and Rowlands MG (1995) Novel steroidal inhibitors of human cytochrome P45017 alpha (17 alpha-hydroxylase-C17,20-lyase): potential agents for the treatment of prostatic cancer. *J Med Chem* **38**:2463–2471.

Schwartz PA, Kuzmic P, Solowiej J, Bergqvist S, Bolanos B, Almaden C, Nagata A, Ryan K, Feng J, Dalvie D, Kath JC, Xu M, Wani R, and Murray BW (2014) Covalent EGFR inhibitor analysis reveals importance of reversible interactions to potency and mechanisms of drug resistance. *Proc Natl Acad Sci U S A* **111**:173–178.

Zhang Z-Y, and Wong YN (2005) Enzyme kinetics for clinically relevant CYP inhibition. *Curr Drug Metab* **6**:241–257.